Article

Fundamental immune–oncogenicity trade-offs define driver mutation fitness

https://doi.org/10.1038/s41586-022-04696-z

Received: 23 January 2021

Accepted: 28 March 2022

Published online: 11 May 2022

Open access

Check for updates

David Hoyos[1,20], Roberta Zappasodi[2,3,4,5,20]✉, Isabell Schulze[2,4], Zachary Sethna[1,6,7], Kelvin César de Andrade[8], Dean F. Bajorin[3,7], Chaitanya Bandlamudi[9,10], Margaret K. Callahan[3,7], Samuel A. Funt[3,7], Sine R. Hadrup[11], Jeppe S. Holm[11], Jonathan E. Rosenberg[3,7], Sohrab P. Shah[1,12], Ignacio Vázquez-García[1], Britta Weigelt[9], Michelle Wu[13], Dmitriy Zamarin[2,3,7], Laura F. Campitelli[14], Edward J. Osborne[14], Mark Klinger[14], Harlan S. Robins[14], Payal P. Khincha[8], Sharon A. Savage[8], Vinod P. Balachandran[3,4,6,7,15], Jedd D. Wolchok[2,3,4,16], Matthew D. Hellmann[3,4,17], Taha Merghoub[2,3,4,16,21]✉, Arnold J. Levine[18,21], Marta Łuksza[19,21] & Benjamin D. Greenbaum[1,12,21]✉

Missense driver mutations in cancer are concentrated in a few hotspots[1]. Various mechanisms have been proposed to explain this skew, including biased mutational processes[2], phenotypic differences[3–6] and immunoediting of neoantigens[7,8]; however, to our knowledge, no existing model weighs the relative contribution of these features to tumour evolution. We propose a unified theoretical 'free fitness' framework that parsimoniously integrates multimodal genomic, epigenetic, transcriptomic and proteomic data into a biophysical model of the rate-limiting processes underlying the fitness advantage conferred on cancer cells by driver gene mutations. Focusing on *TP53*, the most mutated gene in cancer[1], we present an inference of mutant p53 concentration and demonstrate that *TP53* hotspot mutations optimally solve an evolutionary trade-off between oncogenic potential and neoantigen immunogenicity. Our model anticipates patient survival in The Cancer Genome Atlas and patients with lung cancer treated with immunotherapy as well as the age of tumour onset in germline carriers of *TP53* variants. The predicted differential immunogenicity between hotspot mutations was validated experimentally in patients with cancer and in a unique large dataset of healthy individuals. Our data indicate that immune selective pressure on *TP53* mutations has a smaller role in non-cancerous lesions than in tumours, suggesting that targeted immunotherapy may offer an early prophylactic opportunity for the former. Determining the relative contribution of immunogenicity and oncogenic function to the selective advantage of hotspot mutations thus has important implications for both precision immunotherapies and our understanding of tumour evolution.

The distribution of mutations in cancer is highly non-uniform. Mutations in oncogenes and tumour suppressors are enriched across cancers, and specific sites known as hotspots are more frequently mutated, leading to the hypothesis that hotspot mutations offer a selective advantage[1]. A paradigmatic example is the tumour suppressor p53. Although *TP53* is mutated in more than 50% of cancers, only eight hotspot mutations make up approximately one-third of all missense *TP53* mutations[3]. Several hypotheses have been offered to explain the mechanisms behind this skewed distribution, including biased generative mutational processes during tumour evolution[2,3], degree of functional alteration[3–5], structural stability[3,6] and immune editing[7,8]. However, these hypotheses are not mutually exclusive. Mutations and subsequent selection can lead to substantial alterations in the concentration of oncogenic proteins[9–11], a factor that has not been quantified as a contributor to the predominance of hotspot mutations. Generally, mutant p53 is present at a higher concentration than wild-type protein, depending on the tissue, copy-number alteration and mutation[12–14]. Yet, divergence from self and overexpression can contribute to mutant p53 neoantigen immunogenicity, constraining the ability of mutant p53 to avoid immune surveillance. Because neoantigens from mutations in tumour driver genes that are shared across patients and tumour types represent attractive immunotherapeutic targets[15,16], understanding this issue is of critical importance. Here we examine the relationship between oncogenicity and immunogenicity for tumour driver mutations, using p53 as a primary example, to develop a model for predicting therapeutic targeting strategies, such as for neoantigen-based immune therapies.

We found that mutation frequency distributions for commonly mutated driver genes were conserved across multiple cancer mutation databases (Fig. 1a, b) and that innate mutation rates based on

A list of affiliations appears at the end of the paper.

trinucleotide context significantly correlated with mutation frequencies for several genes (Supplementary Information). We next quantified amino acid conservation over homologous proteins, a proxy for functional phenotype (Fig. 1c), and in silico-predicted reduced neoantigen presentation by major histocompatibility complex class I (MHC-I) molecules (Fig. 1d) across driver genes[7]. Several genes have hotspots at conserved sites and are poorly presented (Fig. 1e), implying that the fitness advantages the mutations confer may be driven by both features. We focused on *TP53* because it is widely mutated in tumours, with well-established, order-conserved pan-cancer hotspots (Fig. 1b and Supplementary Table 1) and broadly available functional phenotypic data[5]. We quantified the altered transcription factor function of mutant p53 across eight principal transcriptional targets with a quantitative yeast assay[5] (Fig. 1f and Extended Data Fig. 1). We found that, although loss of transactivation was present for hotspot mutations, many non-hotspot mutations had comparatively low transactivation capacity. Moreover, we predicted MHC-I molecule presentation for the set of nonamer neopeptides surrounding p53 hotspot mutations to be worse than for non-hotspot peptides in The Cancer Genome Atlas (TCGA; $P = 4.748 \times 10^{-7}$, two-sided Welch's *t*-test; Fig. 1g). Mutant p53 loss of transcriptional activity and neoantigen presentation of derived neopeptides showed only weak rank correlation (Fig. 1h), leading us to conclude that all of the mechanisms proposed to underlie mutant p53 fitness are likely to provide some predictive information.

We therefore sought to harmonize this proposed feature set within a mechanistic mathematical model of mutant p53 fitness[17–21]. A model based on background mutation rates alone was insufficient to separate the hotspots from other mutations (Fig. 2a). We further looked to capture variation in mutant p53 concentration, which affects both the transcription factor function and neoantigen presentation. We assigned TCGA samples a normalized p53 protein concentration and effective *MDM2* promoter affinity to infer typical per-allele mutant-specific concentrations[22,23]. We consistently found a significant inverse relationship between these two variables across tumour types (Fig. 2b and Extended Data Fig. 2a) and a significant correlation between our concentration estimates and immunohistochemistry data (Extended Data Fig. 2b, c). We constructed a nonlinear, two-parameter model that separates mutant p53 fitness onto a positive pro-oncogenic probability and a negative immunogenic probability (Supplementary Methods) coupled to mutant p53 concentration. Each component is given an appropriate weight by maximum-likelihood fitting with respect to TCGA mutation frequencies. Our fitness model successfully predicts the distribution of mutation frequencies, both per mutation and per codon (Fig. 2c and Supplementary Information), and accurately predicts the increase or decrease in each mutant frequency with respect to background frequency (Extended Data Fig. 3a, b). We found that predicting the distribution of *TP53* mutations requires both functional and immune components through determining the relative likelihoods of the models (Supplementary Table 2 and Supplementary Methods). Model optimization depended strongly on the sampled MHC-I haplotype and all mutant phenotypes (Extended Data Fig. 3c, d and Supplementary Information). We optimized and applied similar models to other driver genes, with conservation used as a proxy for function (Extended Data Fig. 4a and Supplementary Methods). Combined models were more predictive for mutation distributions with larger frequency variance across all database mutations, which implies that increased mutation frequency variance relates to increased selection, as expected from Fisher's theorem[24] (Extended Data Fig. 4b), such as for *PTEN* (Extended Data Fig. 4c). To build a predictive model for *KRAS*, we were able to include measured binding affinities to the downstream Raf effector protein for a limited set of hotspot mutations[25] (Supplementary Methods), in addition to inferences in conservation and immunogenicity (Extended Data Fig. 4d).

To represent the landscape of mutant p53 fitness, we defined a 'free fitness' function of each mutation as the sum of the positive functional fitness, the negative immune fitness and the logarithm of the background frequency (Supplementary Methods), analogous to a free energy in statistical physics with the multiplicity of states derived from the background mutation rate. We plotted the free fitness landscape (Fig. 2d) and observed a general trade-off between intrinsic fitness (logarithm of the background frequency and functional fitness; Supplementary Methods) and extrinsic immune fitness. The trade-off observed in *TP53* is reminiscent of other evolutionary trade-offs, and we theorized that *TP53* hotspots were Pareto optimal[26,27]. We computed the Pareto front and identified the optimal fitness coordinate constrained by the front when using our model (Fig. 2d and Supplementary Methods). We found that hotspots had statistically higher free fitness (Fig. 2e) and occupied an optimal regime in which they successfully trade off between the pro-tumorigenic benefit of functional loss and the cost of presenting immunogenic neoantigens. However, there was substantial variation among the hotspot mutations. For instance, R175H is functionally the most wild-type-like hotspot but typically has the poorest MHC-I binding capacity. By contrast, the R248Q and R248W (R248Q/W) mutations have nearly complete loss of transcriptional function and therefore can more often afford to generate potentially immunogenic neoantigens, because the proliferative competitive advantage induced by mutation would offset the cost of immunogenicity. For *KRAS*, under more restrictive assumptions, we observed evidence for a trade-off between functional and immune fitness for hotspot mutations in pancreatic adenocarcinoma, where *KRAS* is typically mutated (Extended Data Fig. 4e and Supplementary Methods).

One possible explanation for the inverse relationship is that mutations that alter protein function are generally more likely to generate differentially immunogenic peptides. We therefore compared non-pathogenic and pathogenic mutations in a curated set of non-cancerous disease driver genes and found that both types of mutation generated comparably predicted immunogenic peptides (Extended Data Fig. 5), implying that the trade-off observed is not to be expected a priori. Moreover, because our functional predictions for mutant *TP53* are based on precision yeast assays, we checked for evidence of an oncogenic–immunogenic trade-off using independent TCGA assay for transposase-accessible chromatin with sequencing (ATAC-seq) and RNA sequencing assay to develop a score for the lack of mutant p53 binding site occupancy (Supplementary Methods). We found that the functional component of our fitness model correlated significantly with lack of binding (Extended Data Fig. 6a) and that samples with increased lack of p53 binding consistently showed decreases in p53 target gene RNA expression (Extended Data Fig. 6b). We independently re-derived the oncogenicity–immunogenicity trade-off by comparing the inferred immunogenicity to our scores for lack of binding (Extended Data Fig. 6c). Finally, as a further control, we found a correlation between the yeast assay-derived probability of DNA binding and median target gene RNA expression conditioned on chromatin accessibility (Extended Data Fig. 6d).

We tested our immunogenicity predictions for mutant p53 using peptides from hotspot mutations predicted to be presented on human leukocyte antigen (HLA)-A*02:01 (Supplementary Table 3 and Supplementary Methods), which is the most frequent MHC-I allele in TCGA. First, we asked whether these peptides had differential ability to bind and stabilize HLA on the cell surface, using the TAP2-deficient human lymphoblastoid T2 cell line (Supplementary Methods). We found that R248Q/W peptides but not R175H peptide could significantly stabilize HLA-A*02:01 expression on T2 cells in a dose-dependent manner in comparison with the respective wild-type peptide sequence (Extended Data Fig. 7a and Supplementary Table 3). We next asked whether R175H and R248Q/W *TP53* hotspot mutations elicit differential immune responses in vivo in patients with cancer. We identified seven HLA-A*02:01-positive patients with either bladder or ovarian tumours with these mutations and available peripheral blood mononuclear cell (PBMC) samples at Memorial Sloan Kettering Cancer

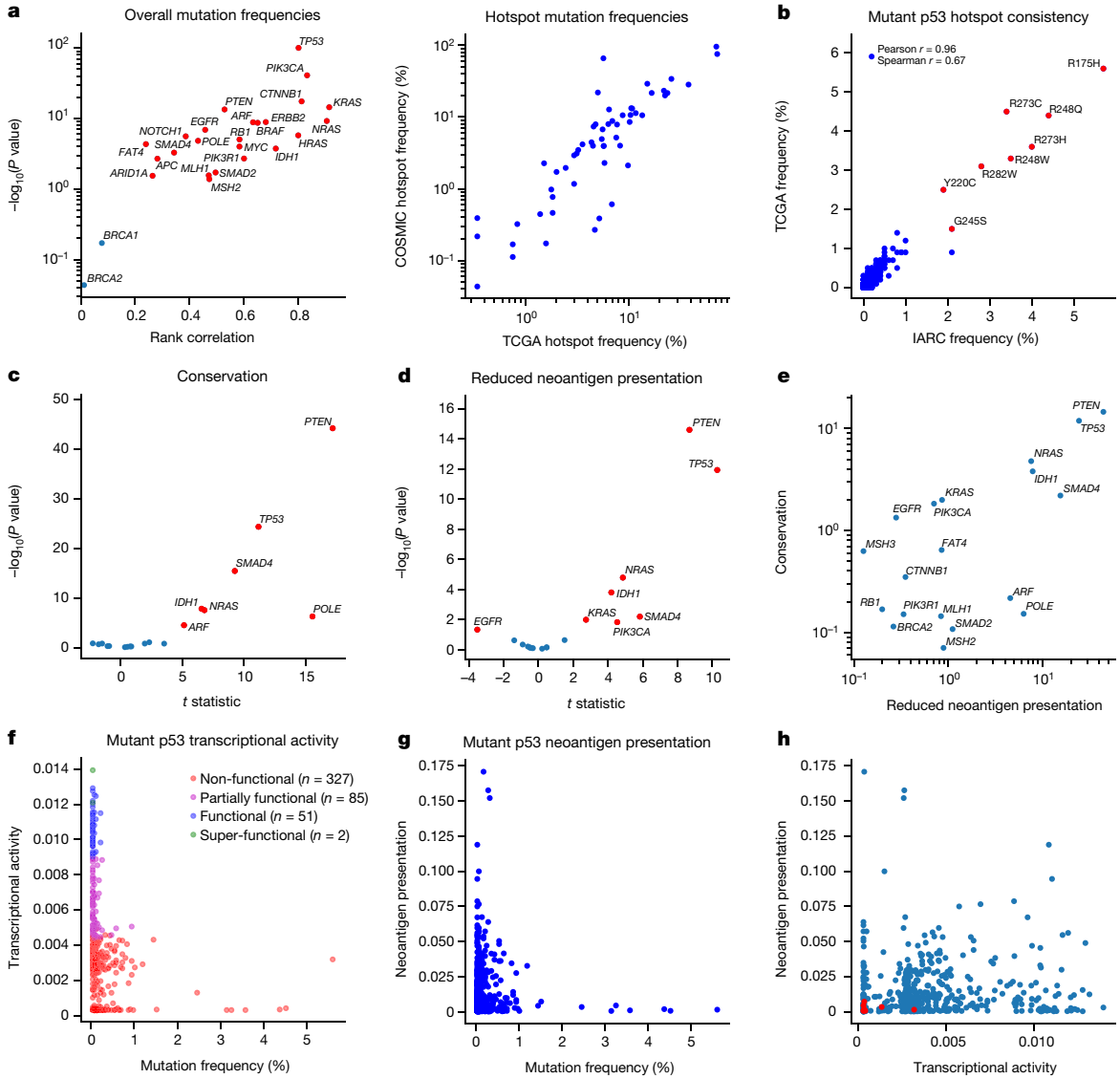

Fig. 1 | Driver gene hotspots are highly conserved and have relatively poor neoantigen presentation. a, Left, rank correlation between shared mutation frequencies in TCGA and the Catalogue of Somatic Mutations in Cancer (COSMIC) database for commonly mutated tumour suppressors and oncogenes plotted against the $-\log_{10}$-transformed rank correlation *P* value. Points corresponding to $P < 0.05$ are coloured red. Right, correlation of individual hotspot mutation frequencies in TCGA and the COSMIC database, excluding TCGA samples (Pearson $r = 0.860$, $P < 0.0001$; Spearman $r = 0.851$, $P < 0.0001$). **b**, Comparison of *TP53* mutation distributions in the TCGA ($n = 2{,}764$) and IARC ($n = 21{,}170$) databases (Pearson $r = 0.963$, $P < 0.0001$; Spearman $r = 0.672$, $P < 0.0001$; labelled hotspots coloured in red). **c**, Comparison of conservation in hotspots and other mutations in the same gene (Welch's *t*-test *P* value, $P < 0.05$ annotated in red). **d**, Comparison of reduced neoantigen presentation between hotspots and other mutations in the same gene (Welch's *t*-test *P* value, $P < 0.05$ annotated in red). **e**, $-\log_{10}$ *P* values from **c** and **d** plotted against each other. **f**, Mutant p53 transcriptional activity defined as the median of the inferred association constant for transcription factor affinity across eight transcriptional targets (*WAF1*, *MDM2*, *BAX*, *h1433s*, *AIP1*, *GADD45*, *NOXA* and *P53R2*) plotted against the frequency of *TP53* mutations in TCGA (Pearson $r = -0.204$, $P < 0.0001$; Spearman $r = -0.404$, $P < 0.0001$). **g**, Neoantigen presentation defined as effective mutant peptide affinity versus mutation frequency in TCGA (Pearson $r = -0.079$, $P = 0.088$; Spearman $r = -0.053$, $P = 0.256$; hotspots coloured in red). **h**, Mutant p53 transcriptional activity plotted against neoantigen presentation shows weak dependence between the two features (Pearson $r = 0.073$, $P = 0.117$; Spearman $r = 0.144$, $P = 0.002$; hotspots coloured in red).

Center (MSKCC). In total, three samples were from patients with R175H-mutant tumours (07E, 38A and 72J) and five samples were from patients with R248Q-mutant tumours (72J, 01A, 39A, 82A and 105A) (Supplementary Table 4). One patient's tumour (72J) had both mutations, although the R175H clonal fraction was far lower (Supplementary Table 4). All but two patients (72J and 07E) were immunotherapy naive at the time of sample collection. Patient 72J, who had a tumour with both hotspot mutations, had an ongoing complete response to nivolumab (anti-programmed death (PD)-1) treatment with no disease detectable at the time of PBMC collection. Patient 07E, who harboured the R175H mutation, was on atezolizumab (anti-PD-L1) treatment at the time of PBMC collection. All other samples were collected before treatment initiation. We stimulated the PBMCs with peptides harbouring the R175H or R248Q mutations or with a CEF (cytomegalovirus, Epstein–Barr virus, and influenza virus) peptide pool or DMSO as positive and negative controls, respectively (Supplementary Table 3). We then measured the interferon-γ (IFNγ) and tumour necrosis factor-α (TNFα) production in $CD8^+$ T cells by flow cytometry (Fig. 3a, b and Extended Data Fig. 7b). We found responses in three of the five R248Q samples, with the response proportional to the size of the $CD8^+$ T cell

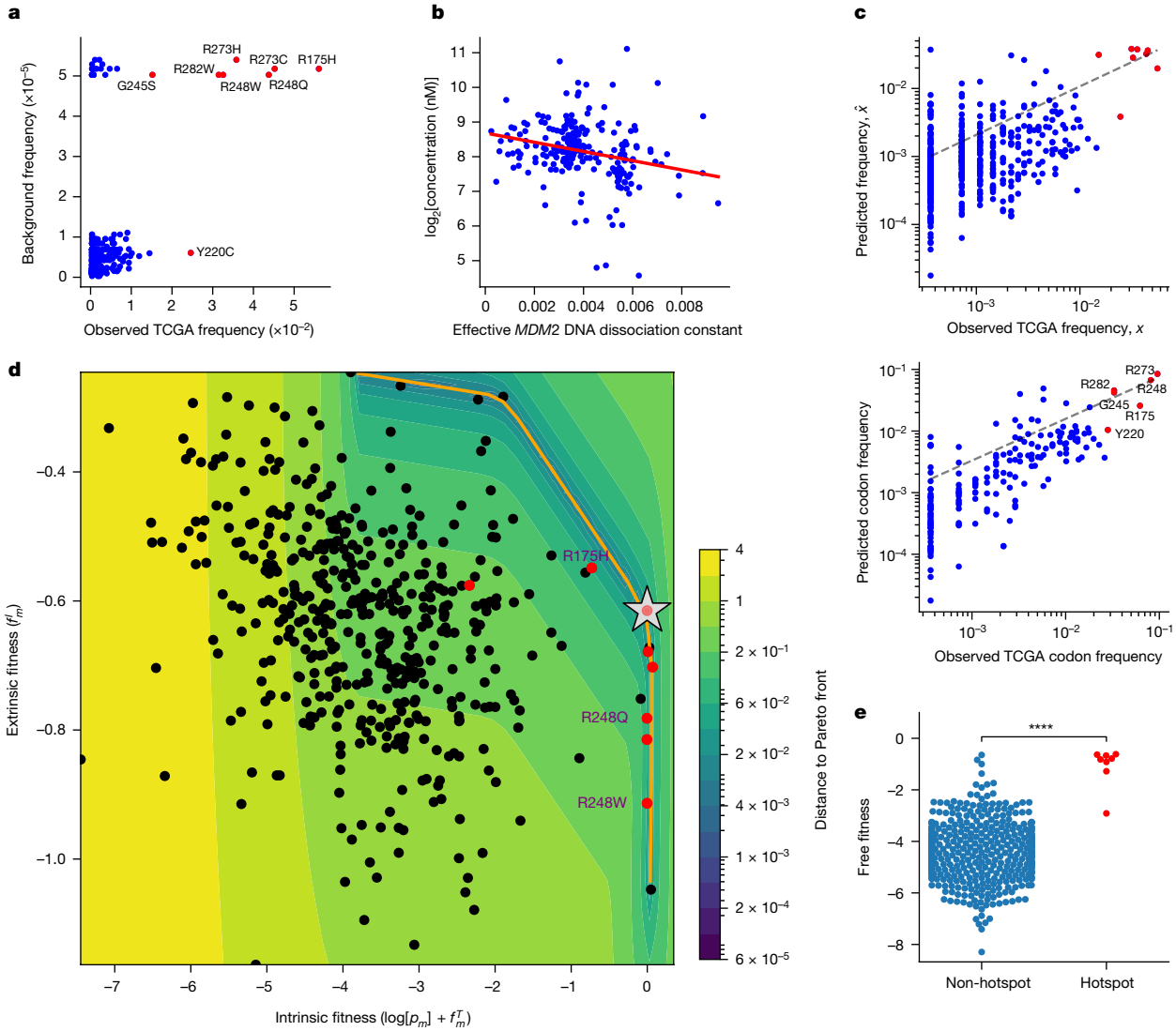

Fig. 2 | Mutant p53 fitness model quantifies the trade-off between oncogenicity and immunogenicity. a, Model with only background intrinsic mutational frequencies (Kullback–Leibler divergence, 1.222; Pearson $r = 0.324$, $P < 0.0001$; Spearman $r = 0.2$, $P < 0.0001$; hotspots coloured in red). **b**, Relationship between mutant p53 concentration ($\log_2$ transformed) and the predicted effective p53 association constant for the *MDM2* promoter across TCGA ($n = 219$; Pearson $r = -0.25$, $P < 0.001$; Spearman $r = -0.29$, $P < 0.0001$). **c**, Correlation of predicted *TP53* mutation frequencies to observed frequencies on a per-mutation basis (top; Kullback–Leibler divergence, 0.599; Pearson $r = 0.671$, $P < 0.0001$; Spearman $r = 0.39$, $P < 0.0001$) and per-protein position basis (bottom; Kullback–Leibler divergence, 0.337; Pearson $r = 0.794$, $P < 0.0001$; Spearman $r = 0.782$, $P < 0.0001$). **d**, Sum of the log-transformed background frequency $\log[p_m]$ and positive functional fitness f_m^T, denoted intrinsic fitness, plotted against negative immune fitness (f_m^I, extrinsic fitness) (Pearson $r = -0.31$, $P < 0.0001$; Spearman $r = -0.33$, $P < 0.0001$). The orange line corresponds to the Pareto front; the silver star indicates optimal free fitness constrained by the Pareto front; and the heat map corresponds to the distance to the Pareto front. The hotspot mutations are coloured red and the R175H and R248Q/W mutations are shown. **e**, Comparison of the free fitness distributions of non-hotspot and hotspot mutations ($P < 0.0001$, Welch's *t*-test).

population (Fig. 3a, b and Extended Data Fig. 7c, d). This indicates responses might correlate with the frequency of $CD8^+$ T cell precursors recognizing the neopeptides. By contrast, only one of the three patients with R175H-mutant tumours had neopeptide reactivity; this patient (07E) had one of the largest expansions for the mutant *TP53* allele and a concomitant increase in protein abundance as well as a positive response to anti-PD-L1 treatment (Fig. 3a and Extended Data Fig. 7e). This finding in combination with the lack of T cell reactivity in the immunotherapy-naive patient (38A) with four mutant R175H alleles indicates despite expansion of the mutant allele, R175H tends to be less immunogenic than R248Q/W, but anti-R175H T cell responses may be unleashed by immune checkpoint blockade therapy. Consistent with this, we found no reactivity in patient 72J, who harboured both hotspot mutations at lower abundance (Extended Data Fig. 7e) and had a complete response to immune checkpoint blockade therapy. This indicates that, in cancer, expansion and/or persistence of cognate T cell pools depends on the levels of the mutant protein.

We next asked whether differential immunogenicity of *TP53* hotspots was a broad phenomenon in the healthy population and therefore potentially linked to the frequency of T cell precursors recognizing a mutant peptide. We compared the capacity of R175H and R248Q/W peptides when loaded onto autologous antigen-presenting cells to prime and expand specific T cells in two healthy donors with the HLA-A*02:01 allele (Extended Data Fig. 7b, Supplementary Table 3 and Supplementary Methods). We consistently noted greater IFNγ and Ki67 expression in T cells stimulated with R248Q/W peptides than in those stimulated with R175H peptides in both donors (Fig. 3c, d and Extended Data Fig. 7f). Furthermore, we assessed the yield of

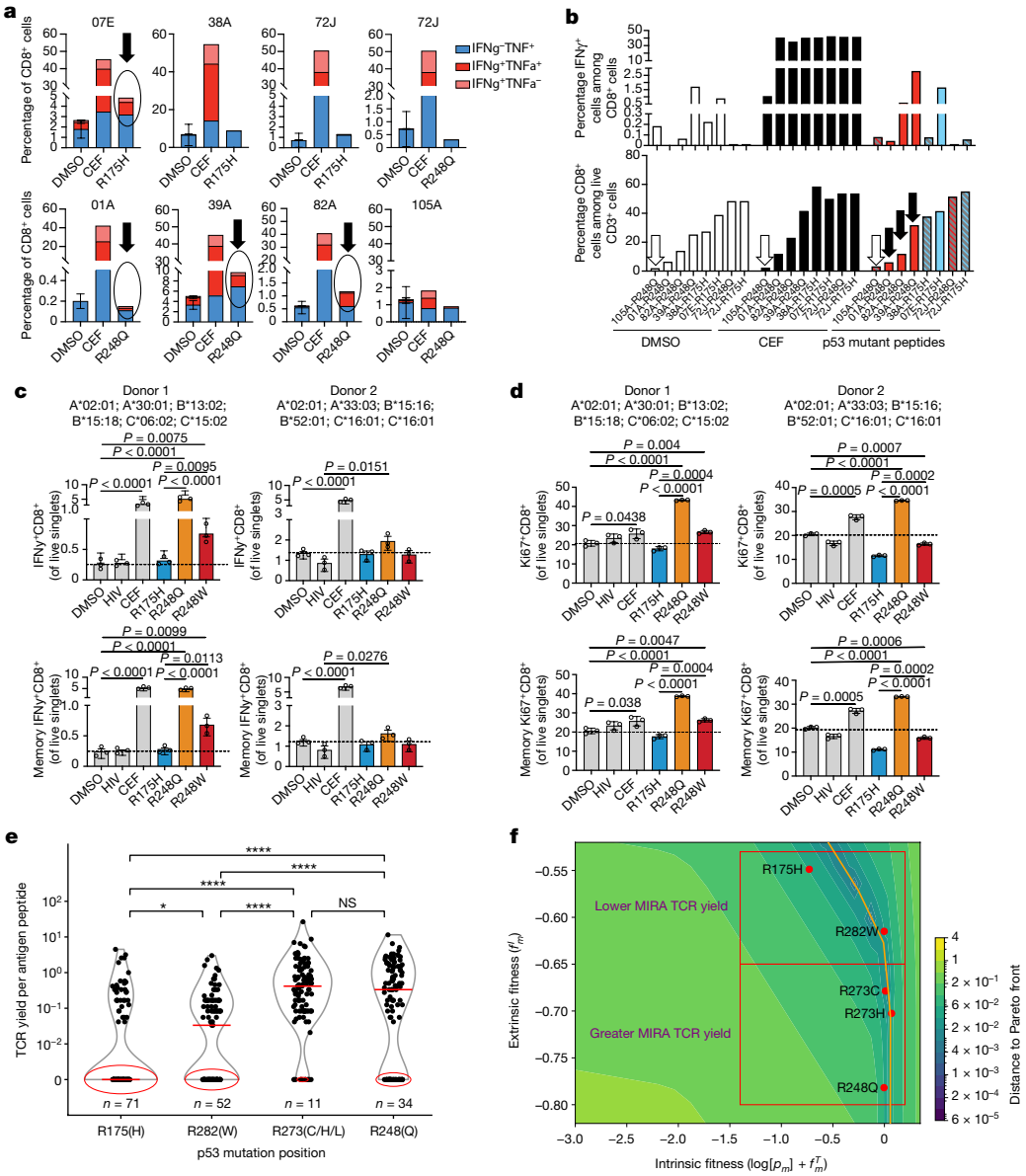

Fig. 3 | Validation of differential reactivity to mutant p53 neoepitopes in healthy donors and patients with cancer. a, **b**, PBMCs from patients with R175H and/or R248Q p53-mutant tumours were cultured with the indicated p53 neopeptides or with CEF or DMSO as positive and negative controls, respectively. **a**, Flow cytometry quantification of cells expressing IFNγ ± TNFα among $CD8^+CD3^+$ live T cells in the indicated samples. DMSO data are the mean ± s.d. of two to three technical replicates. **b**, Assessment of IFNγ responses ($IFN\gamma^+$ cells among $CD8^+$ T cells) in the same samples as in **a** in association with the frequencies of total $CD8^+$ T cells in those cultures. Black arrows indicate reacting samples; a white arrow indicates low-input $CD8^+$ T cells. **c**–**f**, Reactivity of PBMCs from healthy donors to the indicated p53 neoantigens by an optimized ex vivo priming assay (**c**, **d**) and MIRA assay using TCR sequencing to quantify specific T cell clonal expansion (**e**–**f**). IFNγ (**c**) and Ki67 (**d**) expression was assessed in the total $CD8^+$ T cell fraction (top) or the non-naive memory $CD8^+$ T cell fraction (bottom). Frequencies are shown for two individual healthy donors as the percentage of live single cells in culture after 2 weeks of in vitro stimulation with the indicated p53 neopeptides compared with CEF and DMSO or an HIV peptide pool as positive and negative controls, respectively. **e**, Quantification of reactive TCRs in 107 healthy donors in 222 MIRA assay experiments, with an average of two experiments per donor. Median values are denoted by red horizontal line; zero values are circled in red with the number of zero values annotated in blue. **f**, *TP53* hotspots tested in **e** along the Pareto front yielding fewer or more TCRs grouped in red squares. Statistical significance was assessed by unpaired two-sided *t*-tests (**c**, **d**) or Mann–Whitney *U*-test (**e**). $^*P \le 0.05$, $^{**}P \le 0.01$, $^{***}P \le 0.001$, $^{****}P \le 0.0001$.

TP53 hotspot-specific T cell clones by multiplex identification of T cell receptor (TCR) antigen specificity (MIRA) assay (Adaptive Biotechnologies) in PBMC samples from 107 healthy donors representing a set of distinct HLA alleles, including 25 *HLA-A*, 46 *HLA-B* and 20 *HLA-C* alleles (Supplementary Methods). Forty mutant epitopes from R175, R282, R273 and R248 loci covering the top six p53 hotspots were screened for multiple peptide lengths. The distribution of normalized TCR yield per antigen peptide per donor, indicative of specific clonal expansion, was plotted for each hotspot position (Fig. 3e). Notably, we found that the R175 hotspot yielded statistically lower TCR reactivity per peptide as compared with all other hotspots, having a median value of zero reacting TCRs per peptide. Moreover, we found that hotspot reactivity corresponded to fitness model predictions (Fig. 3f). These results indicate that the MHC-I haplotype and TCR repertoire distributions of the healthy population may be more likely to react to the R248 locus than the R175 locus.

Validating the link between increased immunogenicity and immune response to mutant p53, we found that the protein abundance of the

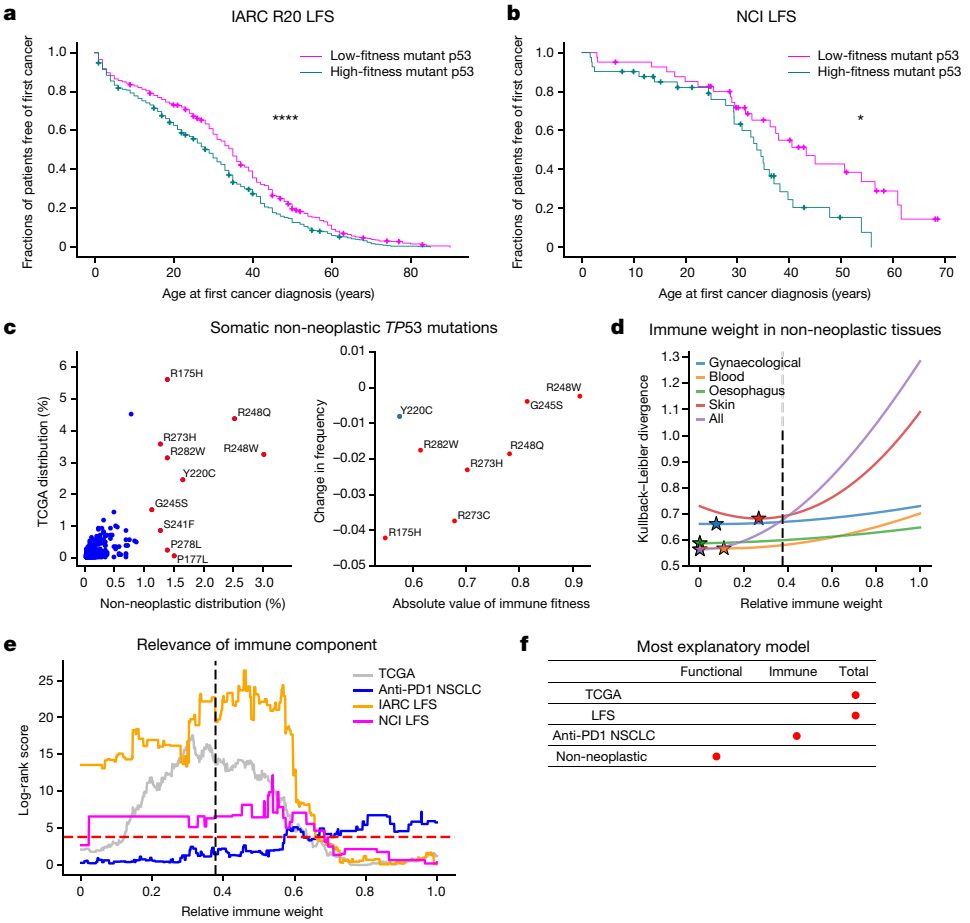

Fig. 4 | Mutant p53 fitness informs LFS age of tumour onset and non-neoplastic *TP53* mutation distribution. a, **b**, Kaplan–Meier curves split on median mutant p53 fitness from the combined model for age of tumour onset in the IARC R20 germline dataset ($n = 998$) (**a**) and the NCI LFS dataset ($n = 82$) (**b**). **c**, Left, comparison of *TP53* mutation frequencies in non-neoplastic tissues (3,451 mutation occurrences) and the frequencies in TCGA (2,764 mutation occurrences; Pearson $r = 0.732$, $P < 0.0001$; Spearman $r = 0.544$, $P < 0.0001$; top 10 non-neoplastic mutations coloured in red and annotated). Right, positive relationship between hotspot frequency difference in non-cancerous and cancerous cells and magnitude of immune fitness. CpG-associated hotspots are coloured in red; Y220C is coloured in blue (overall: Pearson $r = 0.594$, $P = 0.120$; Spearman $r = 0.619$, $P = 0.102$; CpG-associated hotspots only: Pearson $r = 0.827$, $P = 0.022$; Spearman $r = 0.786$, $P = 0.036$). **d**, Kullback–Leibler divergence plotted as a function of relative immune weight for the largest tissue-specific mutation distributions across collected non-neoplastic somatic p53 mutations. Optimal immune weights are denoted as stars, and the optimal relative immune weight derived independently to best represent the observed mutation frequency in TCGA is denoted as a black dotted line. **e**, Log-rank scores of the TCGA ($n = 1,941$), NSCLC ($n = 289$) and LFS (IARC, $n = 946$; NCI, $n = 82$) cohorts as a function of the relative immune weight. The dashed red line corresponds to the log-rank score for $P = 0.05$; the dashed black line marks the choice of parameters trained independently to best represent the observed mutation frequency in TCGA. **f**, The most explanatory models across mutant *TP53* datasets, as indicated by red dots.

CTLA-4, PD-1 and PD-L1 immune checkpoint proteins was higher in TCGA samples with *TP53* mutations that were predicted to be more immunogenic (Extended Data Fig. 8). Our results suggest increased immune activation and concurrent establishment of adaptive immune resistance. When we segregated survival on the basis of functional, immune and combined fitness in TCGA and a cohort of patients with non-small-cell lung cancer (NSCLC) treated with anti-PD-1 at MSKCC (Extended Data Fig. 9), we found that functional and immune fitness components were required to achieve significant survival separation in TCGA, whereas immune fitness on its own significantly separated immunotherapy-treated patients with NSCLC by survival. For robustness, we retrained our models across a range of relative weights between functional and immune fitness (Supplementary Methods). We demonstrated that both components contributed to a model optimized for survival separation across TCGA, with the functional component carrying greater weight, whereas the immune component was the main determinant for an equivalent model in the immunotherapy-treated NSCLC cohort (Fig. 4e).

Because germline *TP53* mutations are the primary cause of Li–Fraumeni syndrome (LFS), which is a highly cancer-prone autosomal dominant disorder[28], we theorized that mutant p53 fitness relates to the time to first tumour formation in patients with LFS. We plotted Kaplan–Meier curves showing the age of tumour onset for persons with germline missense *TP53* mutations in the International Agency for Research on Cancer (IARC) R20 germline dataset and for an independent LFS cohort coordinated by the National Cancer Institute (NCI)[29], stratified on the basis of mutant p53 fitness (Supplementary Methods). We found that functional and immune components were required for significant separation of patients based on time to onset, with the immune component required across a range of relative weights (Fig. 4a, b and Extended Data Fig. 10). These results may seem counterintuitive in that mutant p53 may be interpreted as 'self' by the adaptive immune system in patients with LFS. However, increased mutant p53 abundance, compounded by additional somatic mutations, may increase tumour immune surveillance and mutant p53 antigenicity during tumorigenesis. These findings suggest a possible role for immune

surveillance and the potential for immune intervention in germline *TP53*-mutant tumours.

Finally, non-cancerous cells in diverse tissues harbour somatic *TP53* mutations that confer a competitive advantage, predisposing the clones containing such mutations to develop into cancer[30]. We collated mutation data from multiple published works across many mutated tissues (Supplementary Information) and found the same cancer hotspots in non-neoplastic cells (Fig. 4c). Unexpectedly, however, the frequency of the hotspot mutations was different. R175H was markedly under-represented in non-neoplastic cells compared with tumours ($P < 0.0001$, two-sided binomial test), whereas the potentially more immunogenic R248Q/W mutations were among the most frequent. The addition of an immune component in the non-neoplastic setting improved predictions to a substantially lower degree than in the neoplastic setting (Fig. 4d and Supplementary Table 5), supporting the hypothesis that the difference in hotspot frequency between non-cancerous and cancerous datasets is driven by the hotspot mutation's immune fitness. We then split the non-neoplastic *TP53* mutation dataset into the largest tissue-specific subgroups and found that immune weight depended on the tissue type (Fig. 4d), although the weight was always weaker than the optimal value for fitting the TCGA mutation distribution. Overall, these findings suggest that more functionally fit mutations probably predominate in non-cancerous and precancerous lesions owing to their selective replicative advantage; for cancer to form, however, immune escape becomes critical (Fig. 4f).

We present a general mathematical framework for predicting the fitness of tumour driver mutations. For p53, we used a free fitness model that integrates the background mutation rate, protein concentration, functional fitness advantage and immune fitness cost. Hotspots were predicted to fall on a near-optimal Pareto front, with trade-offs constraining driver mutations from completely evading immune selection, as has been shown for specific hotspot mutations[31–33]. Immune fitness has less of a role in predicting the distribution of non-cancerous *TP53* mutations, which is consistent with recent observations that immune editing is less relevant in precancerous lesions[34]. Our insights therefore help define a window of opportunity for prophylactic immune intervention against mutant p53. Additionally, our model shows that mutant p53 fitness may have a role in determining the age of tumour onset in LFS, implying a benefit in targeting germline *TP53* mutations immunotherapeutically. Inducing prophylactic immunity against mutant p53 seems to be possible according to our in vitro data showing the possibility of inducing anti-mutant p53 T cell responses in healthy individuals and even against poorly immunogenic mutations when sufficient antigen concentration and proper immune co-stimulation are delivered. Our approach captures critical mechanistic determinants of mutant p53 fitness and is amenable to extensions as data become available. For instance, although we considered only functional alterations for a set of canonical p53-regulated genes in this study, future models can include additional new measures for describing mutant gain of function, such as novel binding interactions between mutant p53 and other molecules due to changes in protein conformation or concentration. Similarly, other functions reflecting the vital role of p53 as a central transcription factor may be incorporated with additional data, such as induction of apoptosis at the mitochondria, immune regulation and surveillance of transposons and other genome parasites. The latter evolutionary role of p53 in preserving genome integrity may be responsible for p53's centrality as a bottleneck across transcriptional networks[35–37]. Finally, our free fitness framework lends itself naturally to interpretable, free energy-based machine learning models[38], which broadens the applicability of our approach to additional topics and modalities. By quantifying the underlying mechanisms of driver mutation fitness, we can therefore uncover both fundamental knowledge about tumour evolution and new opportunities for precision therapies.

Online content

Any methods, additional references, Nature Research reporting summaries, source data, extended data, supplementary information, acknowledgements, peer review information; details of author contributions and competing interests; and statements of data and code availability are available at https://doi.org/10.1038/s41586-022-04696-z.

1. Martínez-Jiménez, F. et al. A compendium of mutational cancer driver genes. *Nat. Rev. Cancer* **20**, 555–572 (2020).
2. Giacomelli, A. O. et al. Mutational processes shape the landscape of *TP53* mutations in human cancer. *Nat. Genet.* **50**, 1381–1387 (2018).
3. Baugh, E. H., Ke, H., Levine, A. J., Bonneau, R. A. & Chan, C. S. Why are there hotspot mutations in the *TP53* gene in human cancers? *Cell Death Differ.* **25**, 154–160 (2018).
4. Petitjean, A. et al. Impact of mutant p53 functional properties on *TP53* mutation patterns and tumor phenotype: lessons from recent developments in the IARC *TP53* database. *Hum. Mutat.* **28**, 622–629 (2007).
5. Kato, S. et al. Understanding the function–structure and function–mutation relationships of p53 tumor suppressor protein by high-resolution missense mutation analysis. *Proc. Natl Acad. Sci. USA* **100**, 8424–8429 (2003).
6. Kotler, E. et al. A systematic p53 mutation library links differential functional impact to cancer mutation pattern and evolutionary conservation. *Mol. Cell* **71**, 178–190 (2018).
7. Marty, R. et al. MHC-I genotype restricts the oncogenic mutational landscape. *Cell* **171**, 1272–1283 (2017).
8. Pyke, R. M. et al. Evolutionary pressure against MHC class II binding cancer mutations. *Cell* **175**, 416–428 (2018).
9. Ding, J. et al. Systematic analysis of somatic mutations impacting gene expression in 12 tumour types. *Nat. Commun.* **6**, 8554 (2015).
10. Huang, N., Shah, P. K. & Li, C. Lessons from a decade of integrating cancer copy number alterations with gene expression profiles. *Brief. Bioinform.* **13**, 305–316 (2012).
11. Fehrmann, R. S. et al. Gene expression analysis identifies global gene dosage sensitivity in cancer. *Nat. Genet.* **47**, 115–125 (2015).
12. Köbel, M. et al. Optimized p53 immunohistochemistry is an accurate predictor of *TP53* mutation in ovarian carcinoma. *J. Pathol. Clin. Res.* **2**, 247–258 (2016).
13. Murnyák, B. & Hortobágyi, T. Immunohistochemical correlates of *TP53* somatic mutations in cancer. *Oncotarget* **7**, 64910 (2016).
14. Cole, A. J. et al. Assessing mutant p53 in primary high-grade serous ovarian cancer using immunohistochemistry and massively parallel sequencing. *Sci. Rep.* **6**, 26191 (2016).
15. Tran, E. et al. T-cell transfer therapy targeting mutant *KRAS* in cancer. *N. Engl. J. Med.* **375**, 2255–2262 (2016).
16. Hsiue, E. H. et al. Targeting a neoantigen derived from a common *TP53* mutation. *Science* **371**, eabc8697 (2021).
17. Eigen, M. Selforganization of matter and the evolution of biological macromolecules. *Naturwissenschaften* **58**, 465–523 (1971).
18. Gerland, U. & Hwa, T. On the selection and evolution of regulatory DNA motifs. *J. Mol. Evol.* **55**, 386–400 (2002).
19. Łuksza, M. & Lässig, M. A predictive fitness model for influenza. *Nature* **507**, 57–61 (2014).
20. Balachandran, V. P. et al. Identification of unique neoantigen qualities in long-term survivors of pancreatic cancer. *Nature* **551**, 512–516 (2017).
21. Łuksza, M. et al. A neoantigen fitness model predicts tumour response to checkpoint blockade immunotherapy. *Nature* **551**, 517–520 (2017).
22. Ma, L. et al. A plausible model for the digital response of p53 to DNA damage. *Proc. Natl Acad. Sci. USA* **102**, 14266–14271 (2005).
23. Gaglia, G., Guan, Y., Shah, J. V. & Lahav, G. Activation and control of p53 tetramerization in individual living cells. *Proc. Natl Acad. Sci. USA* **110**, 15497–15501 (2013).
24. Price, G. R. Fisher's 'fundamental theorem' made clear. *Ann. Hum. Genet.* **36**, 129–140 (1972).
25. Hunter, J. C. et al. Biochemical and structural analysis of common cancer-associated *KRAS* mutations. *Mol. Cancer Res.* **13**, 1325–1335 (2015).
26. Shoval, O. et al. Evolutionary trade-offs, pareto optimality, and the geometry of phenotype space. *Science* **336**, 1157–1160 (2012).
27. Pinheiro, F., Warsi, O., Andersson, D. I. & Lässig, M. Metabolic fitness landscapes predict the evolution of antibiotic resistance. *Nat. Ecol. Evol.* **5**, 677–687 (2021).
28. Kratz, C. P. et al. Analysis of the Li–Fraumeni spectrum based on an international germline *TP53* variant data set: an International Agency for Research on Cancer *TP53* database analysis. *JAMA Oncol.* **7**, 1800–1805 (2021).
29. De Andrade, K. C. et al. Cancer incidence, patterns, and genotype–phenotype associations in individuals with pathogenic or likely pathogenic germline *TP53* variants: an observational cohort study. *Lancet Oncol.* **22**, 1787–1798 (2021).
30. Martincorena, I. & Campbell, P. J. Somatic mutation in cancer and normal cells. *Science* **349**, 1483–1489 (2015).
31. Caushi, J. X. et al. Transcriptional programs of neoantigen-specific TIL in anti-PD-1-treated lung cancers. *Nature* **596**, 126–132 (2021).
32. Bear, A. S. et al. Biochemical and functional characterization of mutant KRAS epitopes validates this oncoprotein for immunological targeting. *Nat. Commun.* **12**, 4365 (2021).
33. Malekzadeh, P. et al. Antigen experienced T cells from peripheral blood recognize p53 neoantigens. *Clin. Cancer Res.* **26**, 1267–1276 (2020).
34. Colom, B. et al. Mutant clones in normal epithelium outcompete and eliminate emerging tumours. *Nature* **598**, 510–514 (2021).
35. Wylie, A. et al. *p53* genes function to restrain mobile elements. *Genes Dev.* **30**, 64–77 (2016).
36. Levine, A. J., Ting, D. T. & Greenbaum, B. D. p53 and the defenses against genome instability caused by transposons and repetitive elements. *Bioessays* **38**, 508–513 (2016).

37. McKerrow, W. et al. LINE-1 expression in cancer correlates with *p53* mutation, copy number alteration, and S phase checkpoint. *Proc. Natl Acad. Sci. USA* **119**, e2115999119 (2022).
38. Dayan, P., Hinton, G. E., Neal, R. M. & Zemel, R. S. The Helmholtz machine. *Neural Comput.* **7**, 889–904 (1995).

[1]Computational Oncology, Department of Epidemiology & Biostatistics, Memorial Sloan Kettering Cancer Center, New York, NY, USA. [2]Swim Across America Laboratory and Ludwig Collaborative, Immunology Program, Parker Institute for Cancer Immunotherapy, Memorial Sloan Kettering Cancer Center, New York, NY, USA. [3]Department of Medicine, Weill Cornell Medical College, New York, NY, USA. [4]Parker Institute for Cancer Immunotherapy, Memorial Sloan Kettering Cancer Center, New York, NY, USA. [5]Immunology and Microbial Pathogenesis Program, Weill Cornell Graduate School of Medical Sciences, New York, NY, USA. [6]Hepatopancreatobiliary Service, Department of Surgery, Memorial Sloan Kettering Cancer Center, New York, NY, USA. [7]Department of Medicine, Memorial Sloan Kettering Cancer Center, New York, NY, USA. [8]Division of Cancer Epidemiology and Genetics, Clinical Genetics Branch, National Cancer Institute, National Institutes of Health, Rockville, MD, USA. [9]Department of Pathology and Laboratory Medicine, Memorial Sloan Kettering Cancer Center, New York, NY, USA. [10]Kravis Center for Molecular Oncology, Memorial Sloan Kettering Cancer Center, New York, NY, USA. [11]Experimental and Translational Immunology, Health Technology, Technical University of Denmark, Lyngby, Denmark. [12]Physiology, Biophysics & Systems Biology, Weill Cornell Medicine, Weill Cornell Medical College, New York, NY, USA. [13]Department of Surgery, Memorial Sloan Kettering Cancer Center, New York, NY, USA. [14]Adaptive Biotechnologies, Seattle, WA, USA. [15]David M. Rubenstein Center for Pancreatic Cancer Research, Memorial Sloan Kettering Cancer Center, New York, NY, USA. [16]Human Oncology and Pathogenesis Program, Memorial Sloan Kettering Cancer Center, New York, NY, USA. [17]Thoracic Oncology Service, Memorial Sloan Kettering Cancer Center, New York, NY, USA. [18]Simons Center for Systems Biology, Institute for Advanced Study, Princeton, NJ, USA. [19]Department of Oncological Sciences, Tisch Cancer Institute, Icahn School of Medicine at Mount Sinai, New York, NY, USA. [20]These authors contributed equally: David Hoyos, Roberta Zappasodi. [21]These authors jointly supervised this work: Taha Merghoub, Arnold J. Levine, Marta Łuksza, Benjamin D. Greenbaum. ✉e-mail: roz4022@med.cornell.edu; merghout@mskcc.org; greenbab@mskcc.org

Methods

All research involving human participants was approved by the authors' institutional review board (MSKCC IRB), and all clinical investigation was conducted according to the principles expressed in the Declaration of Helsinki. Written informed consent was obtained from the participants.

Reporting summary

Further information on research design is available in the Nature Research Reporting Summary linked to this paper.

Data availability

Original data required for running the fitness model are available at https://github.com/dfhoyosg/p53_fitness_tradeoff.

Code availability

Original code required for running the fitness model is available at https://github.com/dfhoyosg/p53_fitness_tradeoff.

Acknowledgements We thank U. Alon, C. Chan, N. Copeland, P. Hainaut, N. Jenkins, S. Lowe, D. Pardoll, A. Snyder, D. Ting and the staff of the Balachandran, Greenbaum, Savage and Wolchok laboratories for offering conversations. We also thank N. Rusk for comments and editing. This research was funded in part through National Institutes of Health (NIH)/NCI Cancer Center Support Grant P30CA008748, Swim Across America, the Ludwig Institute for Cancer Research, the Ludwig Center for Cancer Immunotherapy at Memorial Sloan Kettering, the Cancer Research Institute, the Parker Institute for Cancer Immunotherapy, NIH grants R01AI081848, U01CA224175, R01CA240924 and U01CA228963, a collaboration of Stand Up To Cancer, the Society for Immunotherapy of Cancer and the Lustgarten Foundation, the V Foundation for Cancer Research, Sephora and the Pershing Square Sohn Foundation. C.B. was supported by NIH grant R01CA227534-03. D.F.B., S.A.F. and J.E.R. were supported by NIH grant P50CA221745 and the Ludwig Institute for Cancer Research. S.A.F. is supported by NIH grant K12CA184746-01A1. B.D.G. was supported by the Pershing Square Sohn Prize–Mark Foundation Fellowship supported by funding from the Mark Foundation for Cancer Research. M.Ł. is a Pew Biomedical Scholar. The work of K.C.A., P.P.K. and S.A.S. is supported by the Intramural Research Program of the Division of Cancer Epidemiology and Genetics, NCI. S.P.S. was supported by the LesLois Shaw Foundation and holds the Nicholls-Biondi Chair in Computational Oncology at MSKCC. B.W. is funded in part by Breast Cancer Research Foundation and Cycle for Survival grants. R.Z. was supported by the Parker Bridge Fellow Award. D.Z. is supported by the Ovarian Cancer Research Foundation Liz Tilberis Award and the Department of Defense Ovarian Cancer Research Academy (OC150111).

Author contributions B.D.G. conceptualized the study. T.M., A.J.L., M.Ł. and B.D.G. developed the research plan. D.H., Z.S., M.Ł. and B.D.G. developed the computational methodology. R.Z., I.S., A.J.L. and T.M. developed the experimental methodology. D.H., Z.S. and K.C.A. performed the computational analysis. R.Z. and I.S. performed the experimental analysis. P.P.K. and S.A.S. performed the LFS data collection and analysis. S.A.F., J.S.H., J.D.W., M.D.H. and T.M. collected and analysed the human samples. C.B., D.F.B., M.K.C., S.A.F., J.S.H., S.R.H., J.E.R., S.P.S., I.V.-G., B.W., M.W. and D.Z. collected samples from patients with cancer. L.F.C., E.J.O., M.K. and H.S.R. conducted MIRA assays and analysis. D.H., R.Z., I.S., Z.S. T.M., M.Ł. and B.D.G. wrote the manuscript. K.C.A., V.P.B., M.D.H., P.P.K., S.A.S., S.P.S., B.W. and J.D.W. reviewed and edited the manuscript. T.M., A.J.L., M.Ł. and B.D.G. are credited with senior authorship.

Competing interests D.F.B. is a consultant for Bristol Myers Squibb, Merck, Genentech–Roche, AstraZeneca and Pfizer and has received research support from Merck, Genentech–Roche, AstraZeneca, Novartis and Bristol Myers Squibb. M.K.C. has received consulting fees for Bristol Meyers Squibb, Merck, Incyte, Moderna, Immunocore and AstraZeneca and research funding from Bristol Meyers Squibb. L.F.C., E.J.O., M.K. and H.S.R. are employees of Adaptive Biotechnologies. S.A.F. has received research support from AstraZeneca and Genentech–Roche; is a consultant and advisory board member for Merck; and owns stock in UroGen, Allogene Therapeutics, Neogene Therapeutics, Kronos Bio and IconOVir. B.D.G. has received honoraria for speaking engagements from Merck, Bristol Meyers Squibb and Chugai Pharmaceutical; has received research funding from Bristol Meyers Squibb; has been a compensated consultant for PMV Pharma, DarwinHealth and ROME Therapeutics; and is a cofounder of ROME Therapeutics. M.D.H. reports personal fees from Achilles, Adagene, Adicet, Arcus, AstraZeneca, Blueprint, Bristol Myers Squib, Da Volterra, Eli Lilly, Genentech–Roche, Genzyme–Sanofi, Janssen, Immunai, Instil Bio, Mana Therapeutics, Merck, Mirati, Natera, PACT Pharma, Shattuck Labs and Regeneron and has equity options with Factorial, Immunai, Shattuck Labs and Arcus. M.D.H. also reports that a patent filed by Memorial Sloan Kettering related to the use of tumour mutational burden to predict response to immunotherapy (PCT/US2015/062208) is pending and licensed by Personal Genome Diagnostics and that, subsequent to completing this work, he became an employee of AstraZeneca. A.J.L. is a founder, director and shareholder of PMV Pharma and is the chair of the Janssen scientific advisory board. T.M. is a cofounder and holds equity in Imvaq Therapeutics; is a consultant for ImmunOs Therapeutics, Im AQ19 munoGenesis and Pfizer; has received research support from Bristol Myers Squibb, Surface Oncology, Kyn Therapeutics, Infinity Pharmaceuticals, Peregrine Pharmaceuticals, Adaptive Biotechnologies, Leap Therapeutics and Aprea; and has patent applications related to work on oncolytic viral therapy, alpha virus-based vaccines, neoantigen modelling, CD40, GITR, OX40, PD-1 and CTLA-4. I.S. is an inventor on a patent application related to work on CD40. J.E.R. has received consulting fees and trial funding from Bayer, Seagen, AstraZeneca, Roche, Astellas Pharma and QED Therapeutics; consulting fees from Bristol Myers Squibb, Merck, Pfizer, Pharmacyclics, Boehringer Ingelheim, GlaxoSmithKline, Infinity, Janssen, Mirati, EMD Serono, Gilead, BioClin, Eli Lilly and Company, Tyra Biosciences and Pharmacyclics; honoraria for continuing medical education from Research to Practice, MJH Life Sciences, Medscape, Clinical Care Options, OncLive and EMD Serono; royalties from UpToDate. B.W. reports ad hoc membership of the scientific advisory board of Repare Therapeutics, outside the submitted work. J.D.W. is a consultant for Adaptive Biotechnologies, Amgen, Apricity, Ascentage Pharma, ArsenalBio, Astellas, AstraZeneca, Bayer, BeiGene, Boehringer Ingelheim, Bristol Myers Squibb, Celgene, Chugai, Eli Lilly, Elucida, F-Star, Georgiamune, Imvaq, Kyowa Kirin, Linneaus, Merck, Neon Therapeutics, Polynoma, PsiOxus, Recepta, Takara Bio, Trieza, Truvax, SELLAS, Serametrix, Surface Oncology, Syndax, Syntalogic and Werewolf Therapeutics; receives grant and research support from Bristol Myers Squibb and Sephora; and has equity in Tizona Pharmaceuticals, Adaptive Biotechnologies, Imvaq, BeiGene, Linneaus, Apricity, ArsenalBio and Georgiamune. R.Z. is an inventor on patent applications related to work on GITR, PD-1 and CTLA-4; is a scientific advisory board member of iTEOS Therapeutics; has consulted for Leap Therapeutics; and receives grant support from AstraZeneca and Bristol Myers Squibb. D.Z. is a consultant for Merck, Agenus, Hookipa Biotech, AstraZeneca, Western Oncolytics, Synthekine, MANA Therapeutics, Xencor, Memgen and Takeda; receives grant and research support from AstraZeneca, Roche and Plexxikon; holds stock options with ImmunOs Therapeutics, Calidi Biotherapeutics and Accurius; and has a patent related to use of Newcastle disease virus for cancer therapy with royalties paid by Merck.

Additional information
Supplementary information The online version contains supplementary material available at https://doi.org/10.1038/s41586-022-04696-z.
Correspondence and requests for materials should be addressed to Roberta Zappasodi, Taha Merghoub or Benjamin D. Greenbaum.
Peer review information *Nature* thanks Alexander Anderson, Paul Thomas and the other, anonymous, reviewer(s) for their contribution to the peer review of this work.

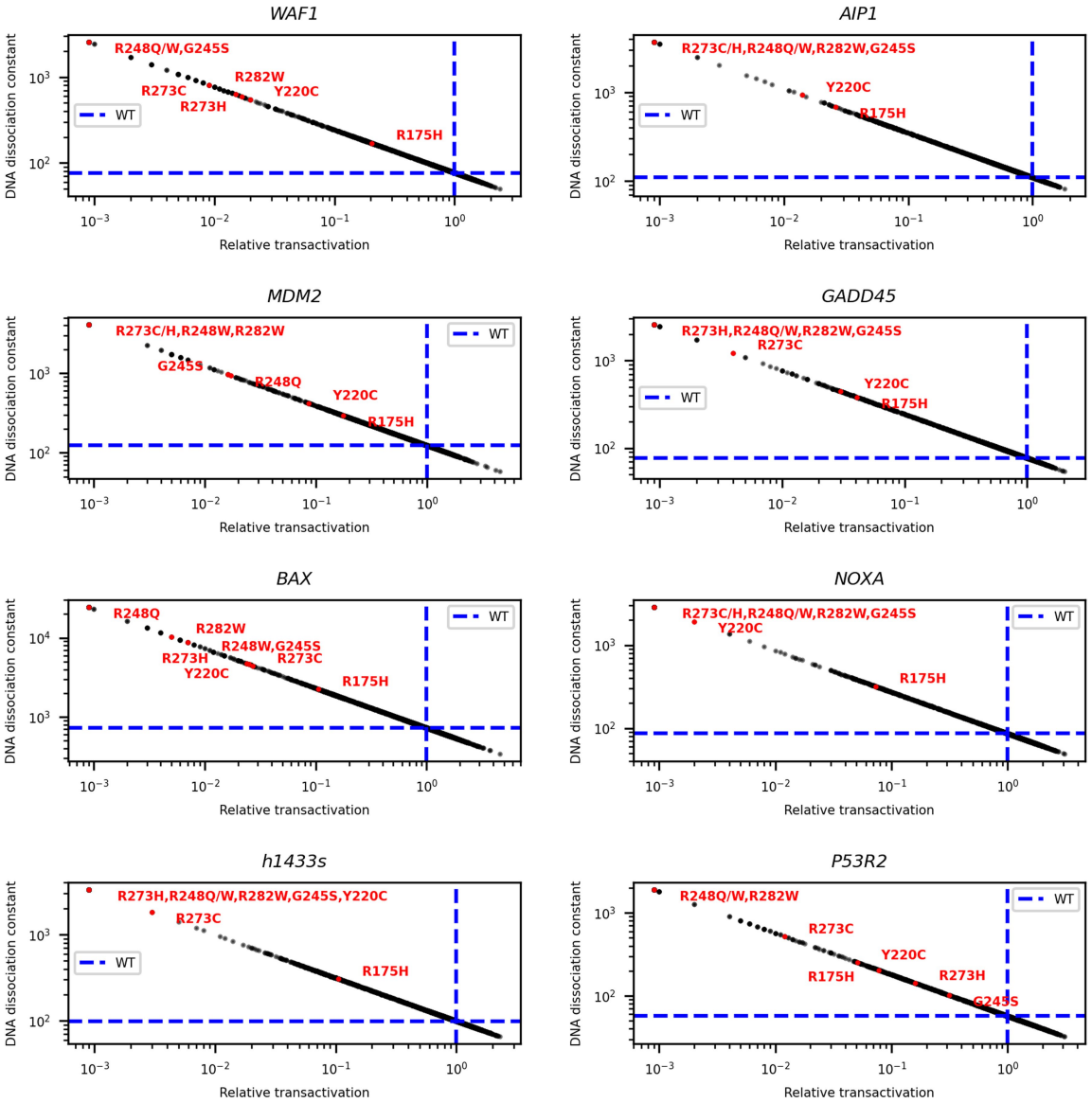

Extended Data Fig. 1 | Inferred relationships between relative transactivation and apparent dimer dissociation constant. Relationship between the relative transactivation and the inferred apparent dimer dissociation constant for mutant homodimer p53. Blue dotted lines correspond to wild-type p53, which has a relative transactivation of 1 (Methods). The hotspots' inferred values are annotated in red.

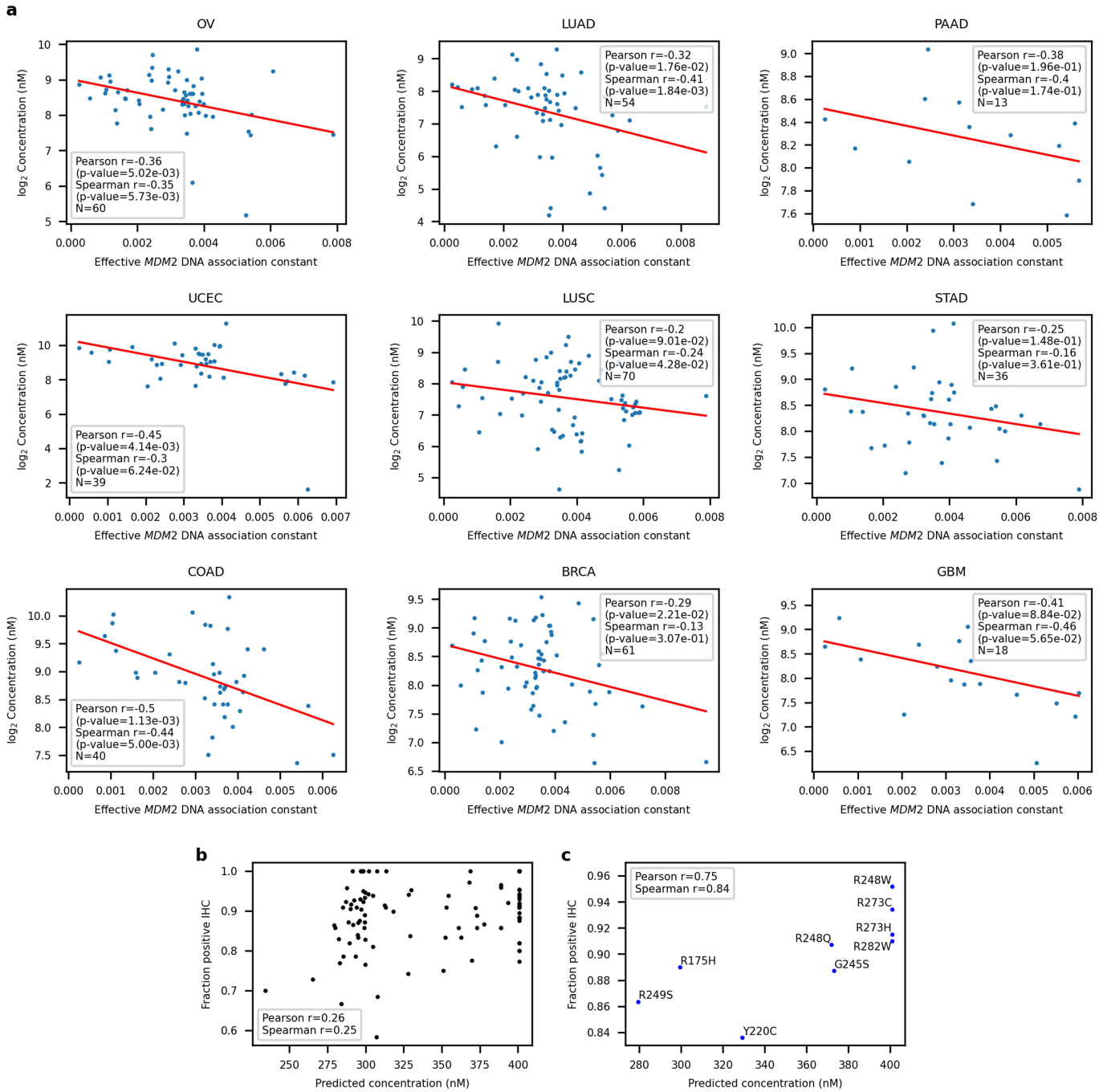

Extended Data Fig. 2 | Relationship between mutant p53 concentration and predicted *MDM2* binding affinities. a, Variation in normalized concentration across mutant p53 versus predicted affinity to *MDM2* DNA in common *TP53*-mutated tissues within TCGA. Protein concentration is expressed as log2 of inferred protein concentration in nanomolar (nM) units. **b**, Fraction positive immunohistochemistry (IHC) assay from the IARC R20 dataset plotted against predicted per-allele mutant p53 concentration averaged across tissues. Correlations are for mutations with at least 10 IHC data entries (Pearson p-value 0.00848, Spearman p-value 0.00967). **c**, Fraction positive IHC assay plotted against predicted per-allele mutant p53 concentration averaged across tissues only for mutant *TP53* hotspots (Pearson p-value 0.0207, Spearman p-value 0.00503).

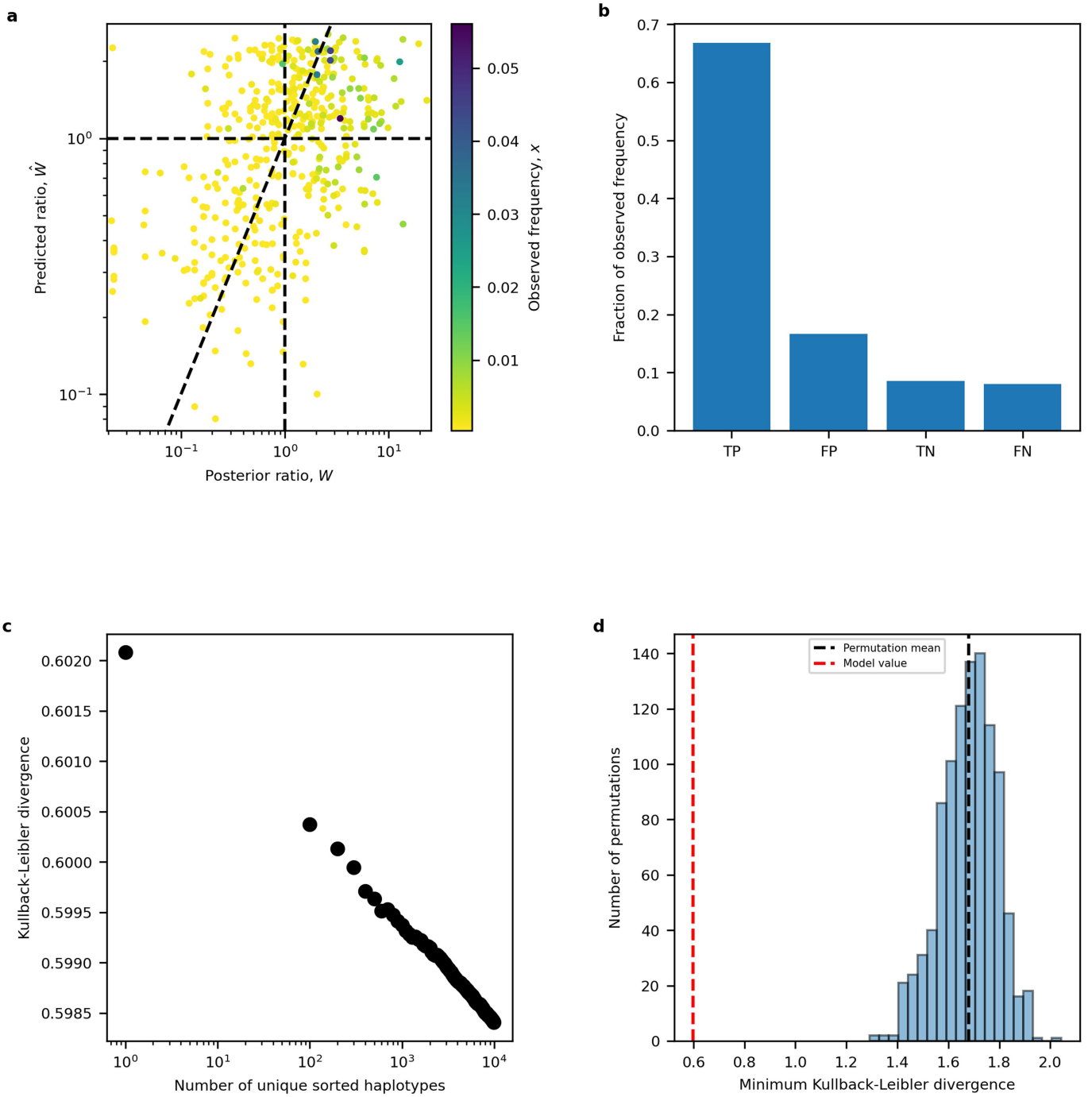

Extended Data Fig. 3 | Fitness model prediction analysis. a, Predicted ratio from combined fitness model plotted against posterior ratio for each *TP53* mutation. Mutations are colored by their observed frequency. Ratios > 1 are predicted to be fixed in the cancer population. Diagonal line corresponds to ratios being equal. **b**, Prediction accuracy plotted as the proportion of observed mutation frequency for true positive (TP), false positive (FP), true negative (TN) and false negative (FN) model predictions. **c**, Kullback-Leiber divergence versus number of simulated HLA-I haplotypes shows improved model predictions according to the haplotype sample size. **d**, Internal validation by shuffling background mutation frequencies, functional phenotypes and immune phenotypes of *TP53* mutations for 1,000 iterations and computing the Kullback-Leibler divergence for each iteration. The histogram is of the distribution of Kullback-Leibler divergences from all iterations. Permutation-mean Kullback-Leibler divergence is plotted as a vertical black dotted line and the true Kullback-Leibler divergence is plotted as a vertical red dotted line.

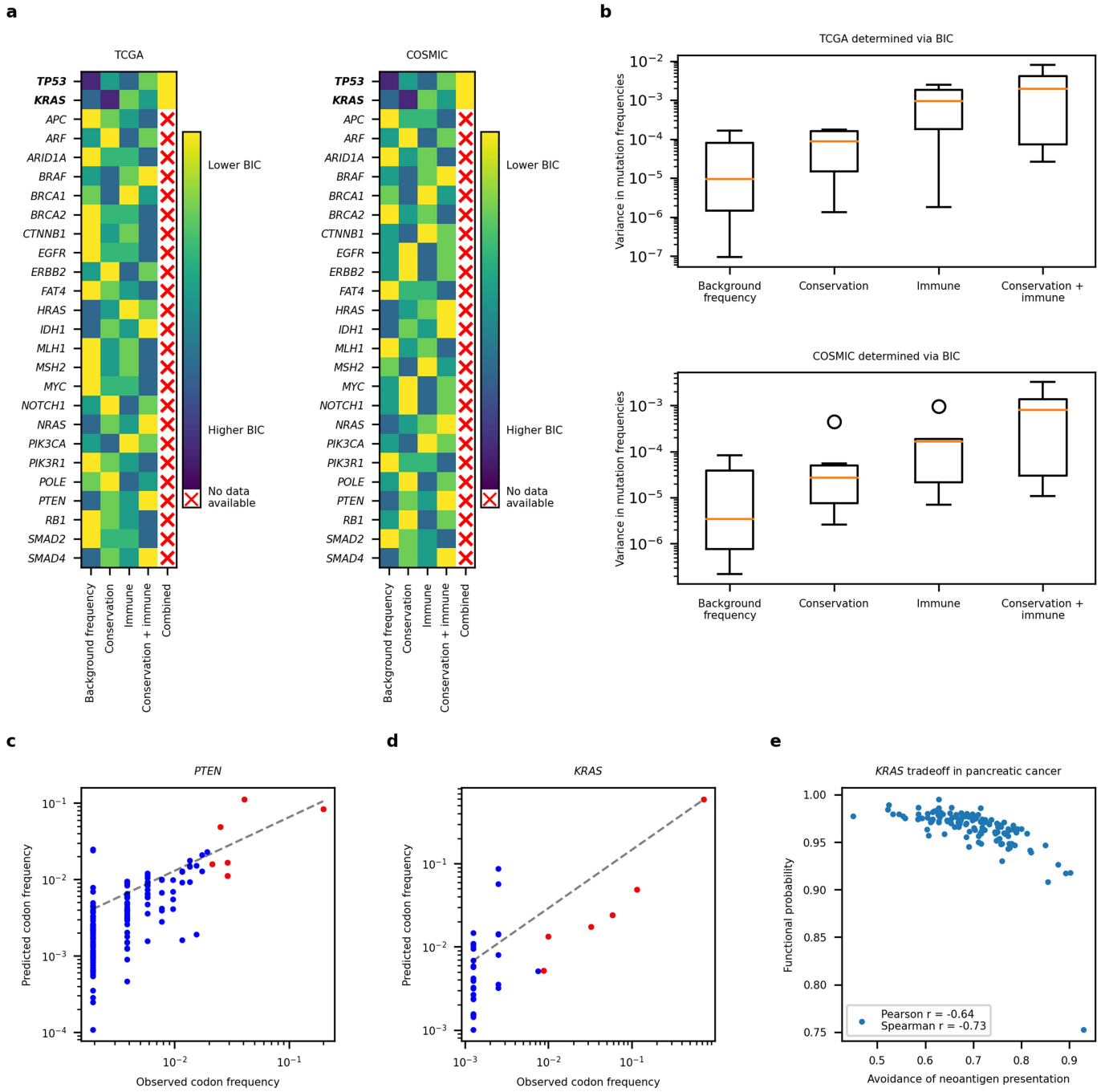

Extended Data Fig. 4 | Fitness model predicts mutation frequencies in commonly mutated cancer driver genes. a, Degree to which models of varying complexity account for mutation distributions from TCGA and COSMIC, excluding TCGA samples, across 27 commonly mutated cancer driver genes. Models are ranked by Bayesian Information Criterion (BIC) in descending order (models with the lowest BIC value are deemed the most explanatory). **b**, Boxplots of observed mutation frequency variances of driver genes best explained by a particular model, ranked by complexity in ascending order. **c**, Fitness model results for *PTEN* per protein position in TCGA, using both conservation and immunogenicity over background mutation rates. The full model is justified by the BIC value (KL divergence = 0.269; Pearson r = 0.701, p-value = 2.013e-24; Spearman r = 0.701, p-value = 2.386e-24). **d**, Fitness model results for *KRAS* per protein position in TCGA, using a full model with conservation, function and immunogenicity over background mutation rates with functional information available for seven frequent *KRAS* cancer mutations (G12A/C/D/R/V, G13D and Q61L). All components are justified by the BIC value (KL divergence = 0.256; Pearson r = 0.981, p-value = 2.095e-24; Spearman r = 0.616, p-value = 0.000104). **e**, Trade-off between gain-of-function and avoidance of neoantigen presentation, defined as $1 - I_m(H)$, in TCGA pancreatic cancer for *KRAS* hotspots (Pearson −0.750, p-value = 2.599e-23; Spearman r = −0.774, p-value = 1.507e-25). Each point corresponds to an individual pancreatic cancer sample with a hotspot *KRAS* mutation.

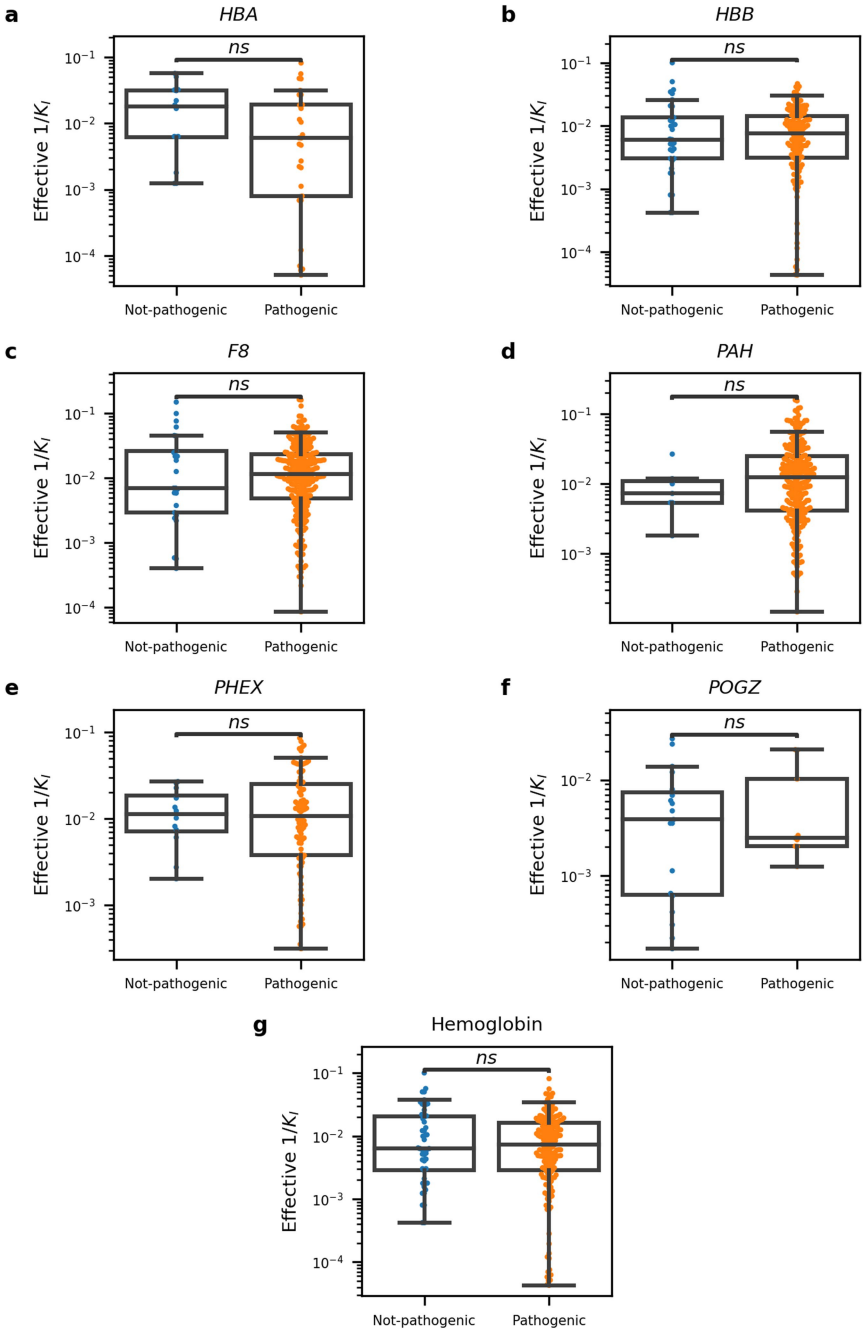

Extended Data Fig. 5 | Inferred mutant immunogenicity is not related to pathogenicity in non-cancer driver genes. a–f, Comparison of inferred immunogenicity across not-pathogenic and pathogenic missense mutations in nine non-cancerous disease driver genes (*HBA*, *HBB*, *HBD*, *HG1*, *HG2*, *F8*, *PAH*, *PHEX* and *POGZ*) using the Mann-Whitney U-test. Six out of nine genes had sufficient data for comparison between not-pathogenic and pathogenic mutations (*HBA*, *HBB*, *F8*, *PAH*, *PHEX* and *POGZ*). **g**, Data corresponding to all hemoglobin subunits (*HBA*, *HBB*, *HBD*, *HG1* and *HG2*) were combined and compared (Hemoglobin). Mutations and their "Not-pathogenic" and "Pathogenic" status were determined using the NCBI's dbSNP and ClinVar systems, respectively.

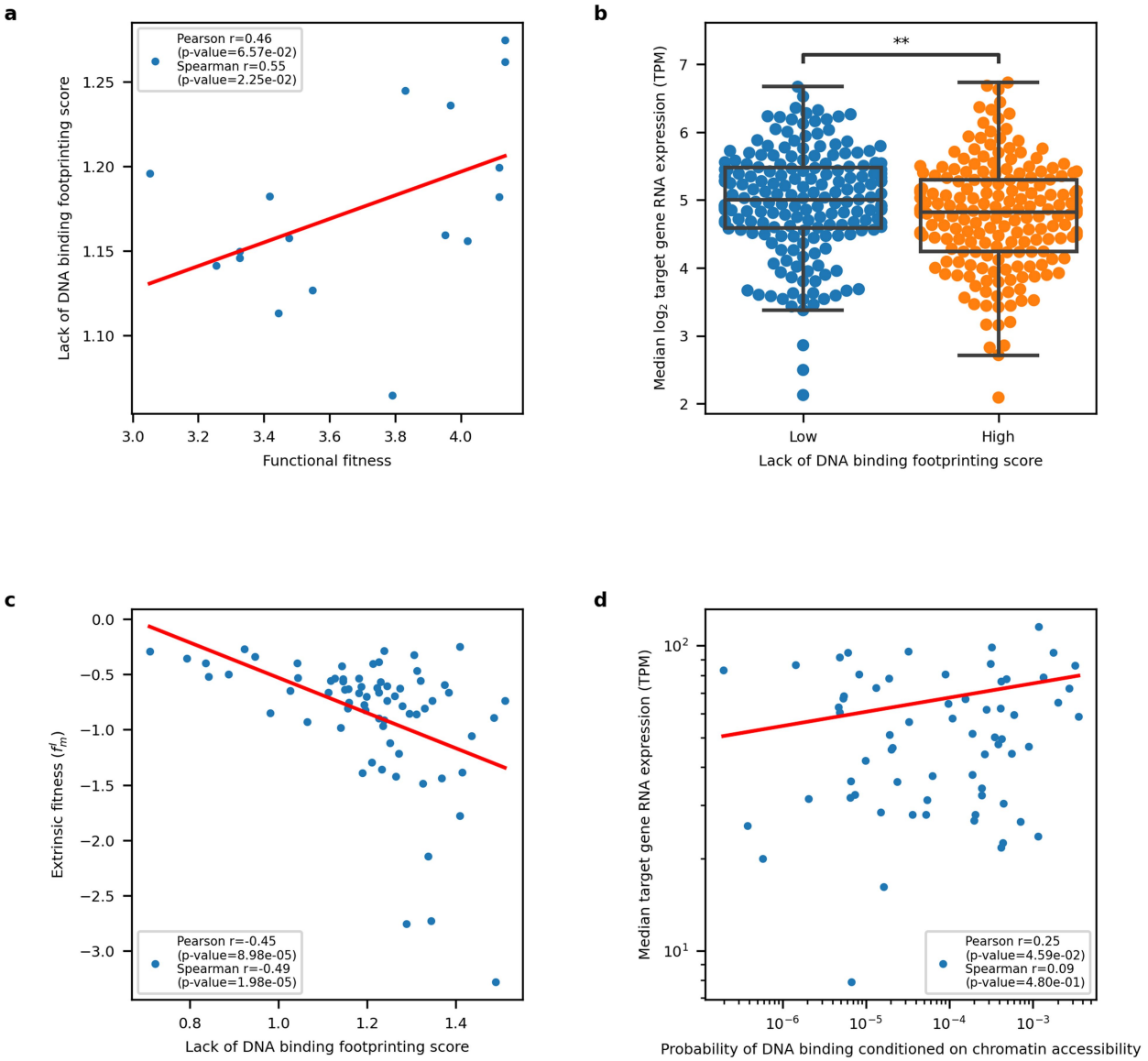

Extended Data Fig. 6 | Fitness trade-offs inferred from ATAC- and RNA-seq. **a**, Lack of binding score plotted versus predicted functional fitness. Most TCGA ATAC-seq samples were breast cancers (BRCA), therefore we only plot matched BRCA samples to normalize on tissue-specific protein abundance (Pearson r = 0.46, p-value = 0.063, Spearman r = 0.55, p-value 0.023, N = 17). **b**, $\log_2$ of median TCGA RNA expression (TPM) of eight p53 target genes utilized in fitness model split on median TCGA ATAC-seq lack of DNA binding score (Mann-Whitney p-value = 0.006). **c**, Immune fitness plotted versus ATAC-seq-based lack of DNA binding footprinting score for each TCGA sample (Pearson r = −0.45, p-value < 0.0001; Spearman r = −0.49, p-value < 0.0001). **d**, Median TCGA RNA expression (TPM) of the target genes with available ATAC-seq data (*WAF1*, *BAX*, *h1433s*, *AIP1*, *GADD45* and *NOXA*) plotted versus median probability of mutant p53 binding DNA, conditioned on target DNA chromatin accessibility (Pearson r = 0.25, p-value 0.0459; Spearman r = 0.088, p-value 0.480).

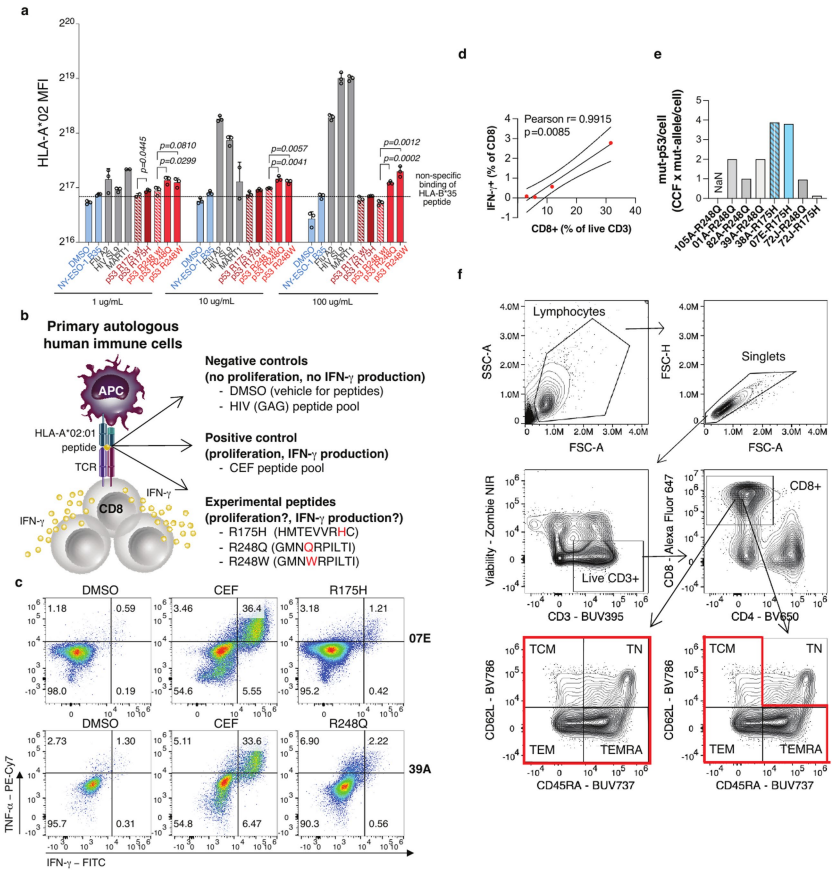

Extended Data Fig. 7 | Differential T-cell reactivity to p53 neopeptides. **a**, Flow cytometry quantification of HLA-A*02:01 expression on the surface of live T2 cells as a measure of peptide:MHC stabilization via binding to specific peptides. T2 cells were incubated overnight in serum-free media with recombinant human B2M and the indicated peptides at the indicated concentrations, or DMSO as vehicle control. Blue, negative controls (DMSO and unrelated HLA-B*35-restricted NY-ESO-1-derived peptide); red, positive controls (HLA-A*02:01-restricted peptides from flu and HIV viral antigens and Mart1/Melan-A melanoma-associated antigen); gray, experimental peptides containing the indicated mutation in comparison with the corresponding wild-type (wt) sequence. Data are mean ± SD of 2-3 replicates. *P* values are calculated with a two-sided unpaired t-test. **b**, Model illustrating the molecular basis of the T-cell stimulation assay and stimulation conditions (APC, antigen presenting cell; TCR, T-cell receptor). **c**, Representative plots of IFN-γ ± TNF-a expressing cells among CD8+CD3+ live T cells in PBMCs from patients with mutant p53 tumors as in Fig. 3a. **d**, Correlation analyses between indicated parameters in PBMC samples from R248Q mutant patients with presence of disease (N = 4) at the time of PBMC collection as in Fig. 3b. **e**, Estimate of mutant p53 amount per tumor cell before treatment in the same patients. Samples with R175H mutations are colored in blue. The sample which reacted, corresponding to the patient who received immune checkpoint blockade (ICB) therapy, is in solid blue, and the sample which did not react, and did not receive ICB, has filled-in lines. **f**, Flow cytometry gating strategy for total CD8 and non-naïve memory CD8 T-cells analyzed in Fig. 3c, d. TN: naïve T-cells, TCM: central memory T-cells, TEM, effector memory T-cells, TEMRA: effector memory T-cells re-expressing CD45RA.

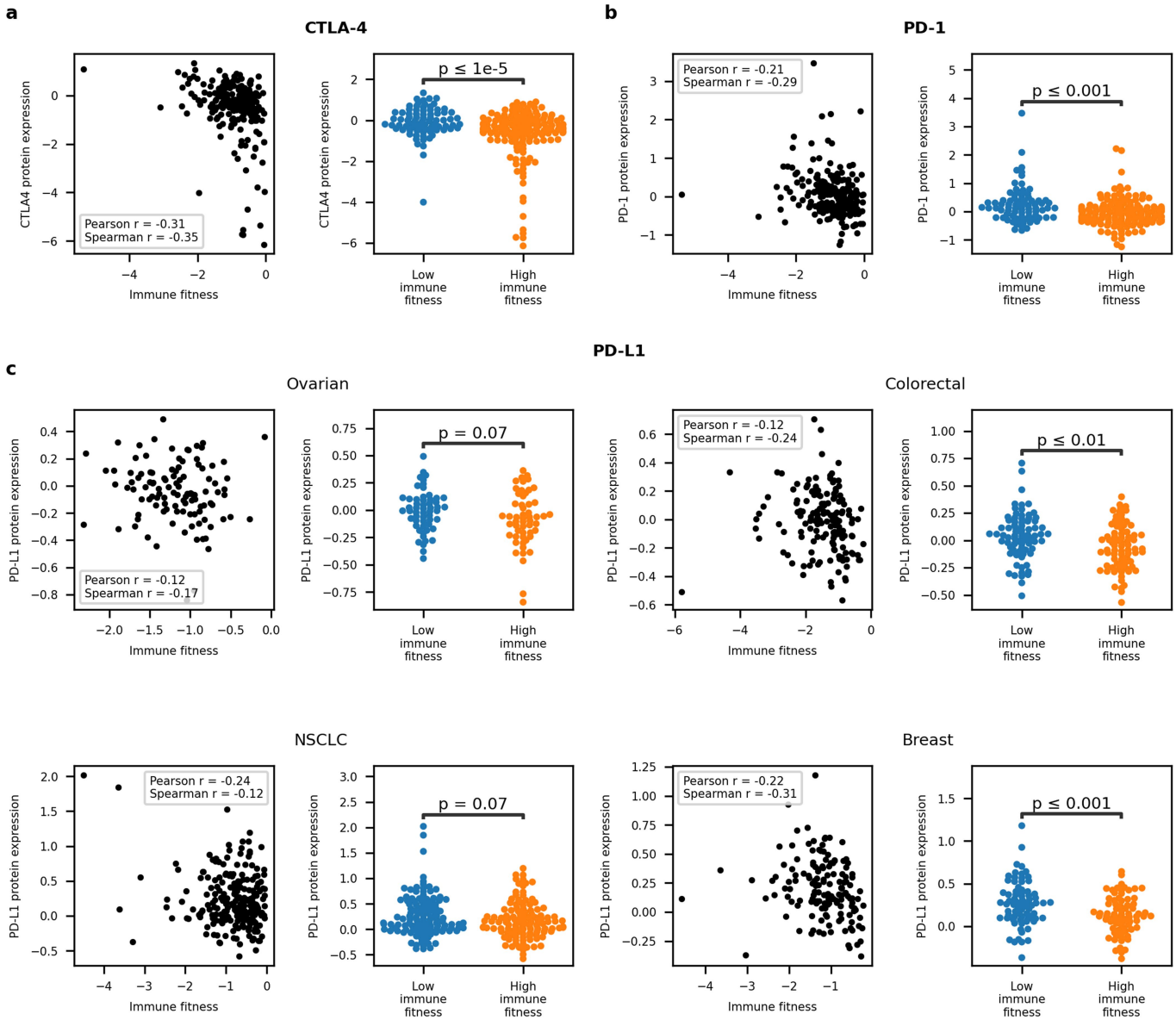

Extended Data Fig. 8 | Relationships between immune fitness and immune checkpoint protein expression in TCGA. a, b, Continuous and categorical relationships between CTLA-4 **(a)** and PD-1 **(b)** protein expression available from TCGA RPPA proteomics assay and immune fitness. For the CTLA-4 scatterplot, Pearson p-value < 0.0001, Spearman p-value < 0.0001. For the PD-1 scatterplot, Pearson p-value = 0.00153, Spearman p-value < 0.0001. Categorical differences measured with the Welch's t-test. **c**, Continuous and categorical relationships between PD-L1 protein expression available from TCGA RPPA proteomics assay and immune fitness in commonly *TP53*-mutated tissues. Correlation p-values: Ovarian - Pearson p-value = 0.2, Spearman p-value = 0.0829; Colorectal - Pearson p-value = 0.157, Spearman p-value 0.003; NSCLC - Pearson p-value = 0.0812, Spearman p-value = 0.00793; Breast - Pearson p-value = 0.00671, Spearman p-value = 0.000140. Categorical differences measured with the Welch's t-test.

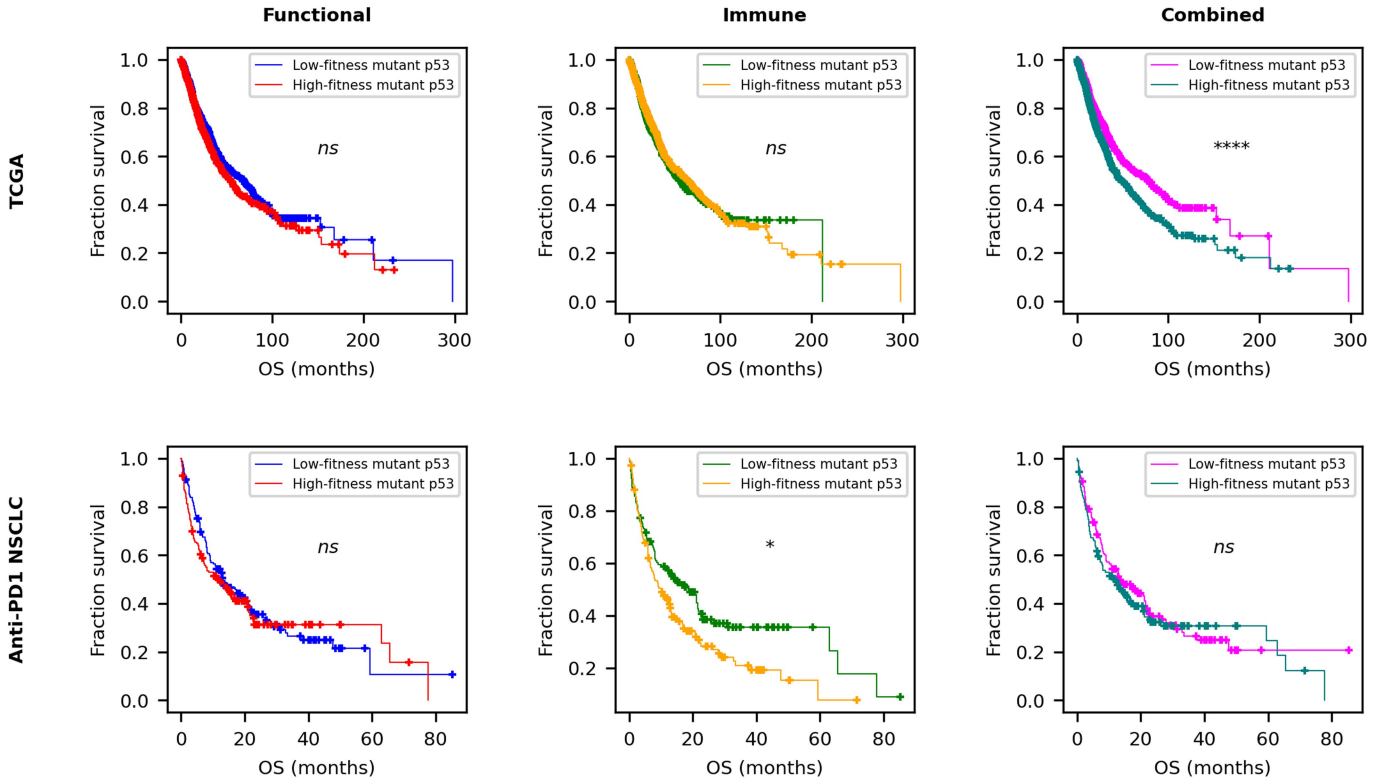

Extended Data Fig. 9 | p53 fitness predicts survival and immune relevance in diverse p53-mutated groups. Kaplan-Meier curves separated by median functional, immune and total fitness in TCGA and MSKCC non-small cell lung cancer (NSCLC) ICB-treated samples. For NSCLC samples, matched HLA-*TP53* mutation pairs with lung-specific and allele-specific concentrations were used to determine functional, immune and combined fitness. *ns* $p > 0.05$, * $p \leq 0.05$, ** $p \leq 0.01$, *** $p \leq 0.001$, **** $p \leq 0.0001$.

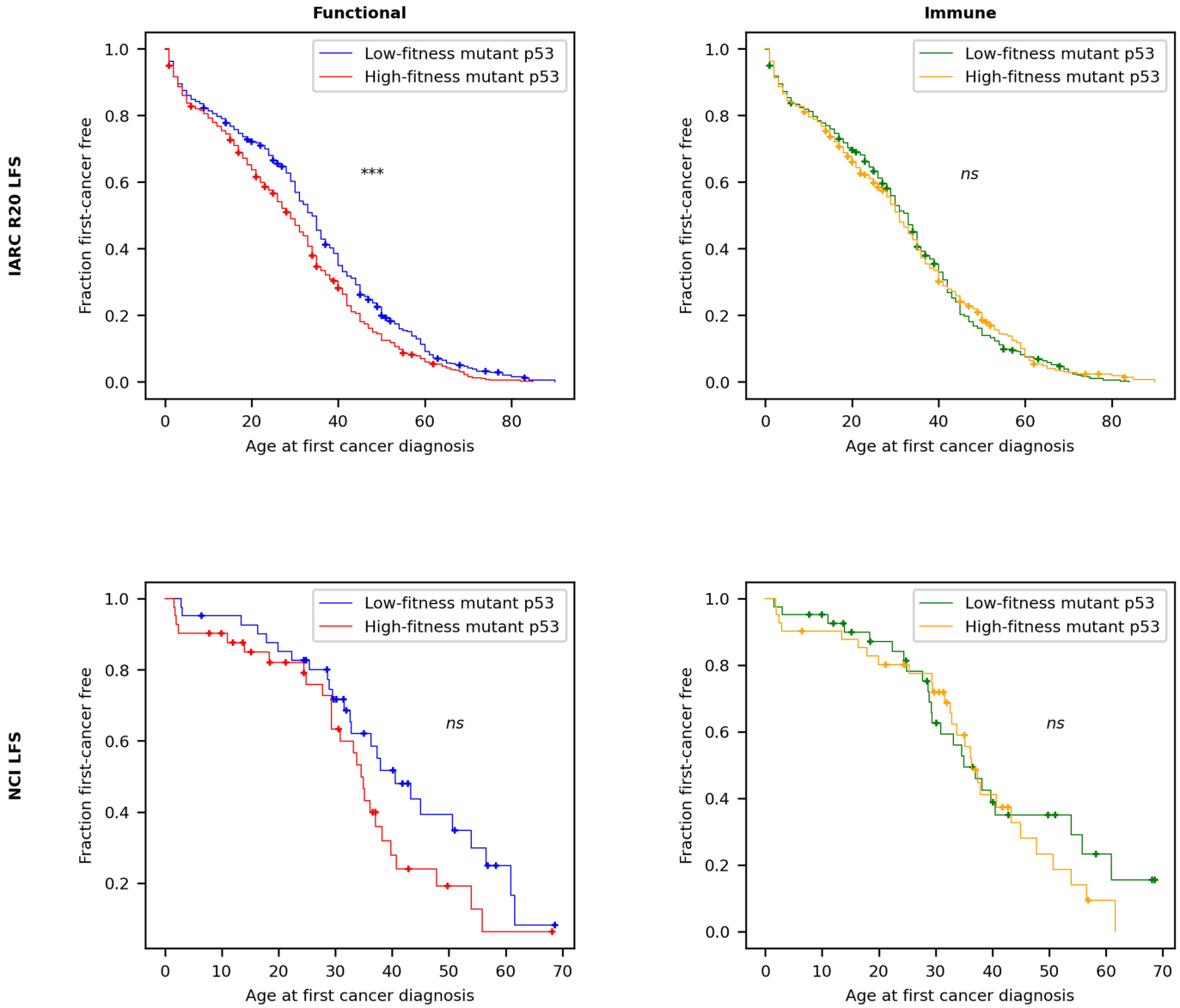

Extended Data Fig. 10 | Relationships of germline mutant p53 fitness and age of tumour onset. Kaplan-Meier curves separated by median functional and immune mutant p53 fitness for first-cancer age of onset in the LFS IARC R20 germline dataset (N = 998) and the NCI LFS cohort (N = 82). Mutant p53 fitness was determined using TCGA-derived tissue-specific mutant p53 concentrations for both datasets, with individual HLA-I types for the NCI cohort and averages taken over TCGA haplotypes for the IARC dataset, which lacked individual HLA-I types.

nature portfolio

Corresponding author(s): Roberta Zappasodi, Taha Merghoub, and Benjamin D. Greenbaum

Last updated by author(s): March 4, 2022

Reporting Summary

Nature Portfolio wishes to improve the reproducibility of the work that we publish. This form provides structure for consistency and transparency in reporting. For further information on Nature Portfolio policies, see our Editorial Policies and the Editorial Policy Checklist.

Statistics

For all statistical analyses, confirm that the following items are present in the figure legend, table legend, main text, or Methods section.

n/a	Confirmed
☐	☒ The exact sample size (*n*) for each experimental group/condition, given as a discrete number and unit of measurement
☐	☒ A statement on whether measurements were taken from distinct samples or whether the same sample was measured repeatedly
☐	☒ The statistical test(s) used AND whether they are one- or two-sided *Only common tests should be described solely by name; describe more complex techniques in the Methods section.*
☐	☒ A description of all covariates tested
☐	☒ A description of any assumptions or corrections, such as tests of normality and adjustment for multiple comparisons
☐	☒ A full description of the statistical parameters including central tendency (e.g. means) or other basic estimates (e.g. regression coefficient) AND variation (e.g. standard deviation) or associated estimates of uncertainty (e.g. confidence intervals)
☐	☒ For null hypothesis testing, the test statistic (e.g. *F*, *t*, *r*) with confidence intervals, effect sizes, degrees of freedom and *P* value noted *Give P values as exact values whenever suitable.*
☐	☒ For Bayesian analysis, information on the choice of priors and Markov chain Monte Carlo settings
☒	☐ For hierarchical and complex designs, identification of the appropriate level for tests and full reporting of outcomes
☐	☒ Estimates of effect sizes (e.g. Cohen's *d*, Pearson's *r*), indicating how they were calculated

Our web collection on statistics for biologists contains articles on many of the points above.

Software and code

Policy information about availability of computer code

Data collection	No software was used to collect data.
Data analysis	Statistical analysis and figures were generated with Python 3. Peptide:HLA-I presentation was inferred in silico using the NetMHC 3.4, NetMHC 4.0, and NetMHCpan 4.1 software. Amino acid conservation was inferred from the ConSurf server and with hmmer 3.3.2, cdhit 4.8.1, MAFFT 7.475, and rate4site 3.0.0. Experimental data was obtain from a 4 laser Aurora full spectrum cytometer (UV-V-B-R, Cytek) and analyzed using the FlowJo software version 10.7.1. Custom code for the fitness model is available at: https://github.com/dfhoyosg/p53_fitness_tradeoff.

For manuscripts utilizing custom algorithms or software that are central to the research but not yet described in published literature, software must be made available to editors and reviewers. We strongly encourage code deposition in a community repository (e.g. GitHub). See the Nature Portfolio guidelines for submitting code & software for further information.

Data

Policy information about availability of data

All manuscripts must include a data availability statement. This statement should provide the following information, where applicable:

- Accession codes, unique identifiers, or web links for publicly available datasets
- A description of any restrictions on data availability
- For clinical datasets or third party data, please ensure that the statement adheres to our policy

The IARC R20 somatic and germline mutation datasets as well as the p53 missense mutation functional information can be downloaded from: https://tp53.isb-cgc.org/.
The somatic p53 non-neoplastic mutations were derived from the referenced publications.
KRAS hotspot functional information derived from the referenced publication.

All TCGA data except RPPA information was downloaded from the Genomic Data Commons: portal.gdc.cancer.gov.
RPPA information was downloaded from the TCPA portal: tcpaportal.org/tcpa/download.html.
The gene DNA sequences were downloaded from: https://www.ncbi.nlm.nih.gov.
The gene protein product sequences were downloaded from UniProt: https://www.uniprot.org.
COSMIC mutation frequencies were downloaded from COSMIC: cancer.sanger.ac.uk/cosmic.
Simulated HLA-I haplotypes were derived using HLA-I frequencies derived from the National Marrow Donor Program: allelefrequencies.net.
Original data required for running the fitness model is available at: https://github.com/dfhoyosg/p53_fitness_tradeoff.

Field-specific reporting

Please select the one below that is the best fit for your research. If you are not sure, read the appropriate sections before making your selection.

☒ Life sciences ☐ Behavioural & social sciences ☐ Ecological, evolutionary & environmental sciences

For a reference copy of the document with all sections, see nature.com/documents/nr-reporting-summary-flat.pdf

Life sciences study design

All studies must disclose on these points even when the disclosure is negative.

Sample size	Sample sizes were dependent on the availability of data. In all cases, we used samples with SNV-derived missense mutations. Our framework takes into account sample size when predicting mutation frequencies and model complexity. Since we considered driver genes which are well-known to be often mutated in cancer, we deemed these sample sizes sufficient.
Data exclusions	All non-SNV-derived missense mutations were excluded from the analysis in all cases. We also excluded the well-known codon 72 and 46 p53 polymorphisms involving proline/arginine and proline/serine amino acids, respectively. For the National Cancer Institute germline p53 mutation cohort, non-melanoma skin cancers and HPV-associated high grade dysplasias were excluded.
Replication	Antigen presentation experiments were repeated three times each for each peptide:HLA-I prediction. All repetition attempts were successful. For each repetition the results were consistent, and the standard error bars are shown.
Randomization	For experiments, two donors without a history of cancer with the HLA-A*02:01 HLA-I molecule were chosen to test presentation of antigens by this HLA-I molecule. We also inferred presentation of the examined peptides from the other present HLA-I molecules within the two donors, and found that, where prediction allowed, none of the present HLA-I molecules were able to present the tested peptides. For the MIRA experiments, random healthy donor PBMCs were utilized. Cancer samples were determined by sample availability.
Blinding	Blinding was not relevant to our study since we were interested in testing the prediction that there would be differential presentation of p53 hotspots neoantigens.

Reporting for specific materials, systems and methods

We require information from authors about some types of materials, experimental systems and methods used in many studies. Here, indicate whether each material, system or method listed is relevant to your study. If you are not sure if a list item applies to your research, read the appropriate section before selecting a response.

Materials & experimental systems

n/a	Involved in the study
☐	☒ Antibodies
☒	☐ Eukaryotic cell lines
☒	☐ Palaeontology and archaeology
☒	☐ Animals and other organisms
☐	☒ Human research participants
☐	☒ Clinical data
☒	☐ Dual use research of concern

Methods

n/a	Involved in the study
☒	☐ ChIP-seq
☐	☒ Flow cytometry
☒	☐ MRI-based neuroimaging

Antibodies

Antibodies used	For RPPA analysis: p53 antibody #9282 (Cell Signaling Technology). For the experiments: anti-human CD3-BUV395 (BD Biosciences, cat. no. 740283), anti-human CD4-AlexaFluor700 (Invitrogen, cat. no. 56-0047-42), anti-human CD8-AlexaFluor647 (BD Biosciences, cat. no. 557708), anti-human CD45RA-BUV737 (BD Biosciences, cat. no. 564442), anti-human CD62L-PE (BD Biosciences, cat. no. 555544), anti-human IFN-γ-FITC (Invitrogen, cat. no. BMS107FI), and anti-human Ki67-APC-eFluor 780 (Invitrogen, cat. no. 47-5698-82).
Validation	The p53 antibody #9282 (Cell Signaling Technology) has been validated using SimpleChIP® Enzymatic Chromatin IP Kits (https://

Validation	www.cellsignal.com/products/primary-antibodies/p53-antibody/9282). For details regarding validation for the experimental antibodies, please see the relevant references on the appropriate websites: https://www.bdbiosciences.com/us/reagents/research/antibodies-buffers/immunology-reagents/anti-human-antibodies/cell-surface-antigens/buv395-mouse-anti-human-cd3-hit3a/p/740283 https://www.thermofisher.com/antibody/product/CD4-Antibody-clone-SK3-SK-3-Monoclonal/56-0047-42 https://www.bdbiosciences.com.com/eu/reagents/research/antibodies-buffers/immunology-reagents/anti-human-antibodies/cell-surface-antigens/alexa-fluor-647-mouse-anti-human-cd8-rpa-t8/p/557708 https://www.bdbiosciences.com/us/reagents/research/antibodies-buffers/immunology-reagents/anti-human-antibodies/cell-surface-antigens/buv737-mouse-anti-human-cd45ra-hi100/p/612846 https://www.bdbiosciences.com/us/applications/research/t-cell-immunology/regulatory-t-cells/surface-markers/human/pe-mouse-anti-human-cd62l-dreg-56/p/555544 https://www.thermofisher.com/antibody/product/IFN-gamma-Antibody-clone-GZ-4-Monoclonal/BMS107FI https://www.thermofisher.com/antibody/product/Ki-67-Antibody-clone-SolA15-Monoclonal/47-5698-82

Human research participants

Policy information about studies involving human research participants

Population characteristics	The National Cancer Institute germline p53 mutation cohort consisted of 82 individuals. As of March 24, 2020, 52 individuals had at least one cancer while 30 had remained cancer-free. Additional information is available in the Methods section. Cancer patients had ovarian and bladder cancer.
Recruitment	Participants or their legal guardians signed informed consent, completed questionnaires, and provided medical records, including pathology and genetic testing reports to validate cancer diagnoses and TP53 variant, as previously described (Mai et al., 2016, Cancer). Cancer samples were determined by availability.
Ethics oversight	The National Cancer Institute's and Memorial Sloan Kettering Cancer Center's Institutional Review Board.

Note that full information on the approval of the study protocol must also be provided in the manuscript.

Clinical data

Policy information about clinical studies

All manuscripts should comply with the ICMJE guidelines for publication of clinical research and a completed CONSORT checklist must be included with all submissions.

Clinical trial registration	NCT01443468
Study protocol	https://clinicaltrials.gov/ct2/show/NCT01443468
Data collection	Data began to be collected on September 29, 2011.
Outcomes	Age of cancer onset was the primary outcome measure used for the Kaplan-Meier survival analysis.

Flow Cytometry

Plots

Confirm that:

☒ The axis labels state the marker and fluorochrome used (e.g. CD4-FITC).

☒ The axis scales are clearly visible. Include numbers along axes only for bottom left plot of group (a 'group' is an analysis of identical markers).

☒ All plots are contour plots with outliers or pseudocolor plots.

☒ A numerical value for number of cells or percentage (with statistics) is provided.

Methodology

Sample preparation	Human peripheral mononuclear cells for in vitro assays were collected from HLA-I typed healthy donors under approved protocols. Refer to the methods for further details.
Instrument	Data was acquired on a 4 laster Aurora full spectrum cytometer (UV-V-B-R, Cytek).
Software	FlowJo software (version 10.7.1).

Cell population abundance	CD4 and CD8 cells were enriched by magnetic separation (>90% purity). Dendritic cells were differentiated from CD14+ monocytes in vitro reaching >80% purity.
Gating strategy	The gating strategy is fully displayed in Extended Data Figure 7.

☒ Tick this box to confirm that a figure exemplifying the gating strategy is provided in the Supplementary Information.